UPPSALA
UNIVERSITET

Rosetta spacecraft potential and activity evolution of comet 67P

by

Elias Odelstad

May 12, 2016

DEPARTMENT OF PHYSICS AND ASTRONOMY
UPPSALA UNIVERSITY
SE-75120 UPPSALA, SWEDEN

Abstract

The plasma environment of an active comet provides a unique setting for plasma physics research. The complex interaction of newly created cometary ions with the flowing plasma of the solar wind gives rise to a plethora of plasma physics phenomena, that can be studied over a large range of activity levels as the distance to the sun, and hence the influx of solar energy, varies. In this thesis, we have used measurements of the spacecraft potential by the Rosetta Langmuir probe instrument (LAP) to study the evolution of activity of comet 67P/Churyumov-Gerasimenko as it approached the sun from 3.6 AU in August 2014 to 2.1 AU in March 2015. The measurements are validated by cross-calibration to a fully independent measurement by an electrostatic analyzer, the Ion Composition Analyzer (ICA), also on board Rosetta.

The spacecraft was found to be predominantly negatively charged during the time covered by our investigation, driven so by a rather high electron temperature of ~ 5 eV resulting from the low collision rate between electrons and the tenuous neutral gas. The spacecraft potential exhibited a clear covariation with the neutral density as measured by the ROSINA Comet Pressure Sensor (COPS) on board Rosetta. As the spacecraft potential depends on plasma density and electron temperature, this shows that the neutral gas and the plasma are closely coupled. The neutral density and negative spacecraft potential were higher in the northern hemisphere, which experienced summer conditions during the investigated period due to the nucleus spin axis being tilted toward the sun. In this hemisphere, we found a clear variation of spacecraft potential with comet longitude, exactly as seen for the neutral gas, with coincident peaks in neutral density and spacecraft potential magnitude roughly every 6 h, when sunlit parts of the neck region of the bi-lobed nucleus were in view of the spacecraft. The plasma density was estimated to have increased during the investigated time period by a factor of 8-12 in the northern hemisphere and possibly as much as a factor of 20-44 in the southern hemisphere, due to the combined effects of seasonal changes and decreasing heliocentric distance.

The spacecraft potential measurements obtained by LAP generally exhibited good correlation with the estimates from ICA, confirming the accuracy of both of these instruments for measurements of the spacecraft potential.

List of papers

This thesis is based on the following papers, which are referred to in the text by their Roman numerals.

I *Evolution of the plasma environment of comet 67P from spacecraft potential measurements by the Rosetta Langmuir probe instrument*
   E. Odelstad, A. I. Eriksson, N. J. T. Edberg, F. Johansson, E. Vigren, M. André , C.-Y. Tzou, C. Carr, and E. Cupido
   Geophysical Research Letters 42, 126-134, 2015

II *Measurements of the electrostatic potential of Rosetta at comet 67P*
   E. Odelstad, G. Stenberg-Wieser, M. Wieser, A. I. Eriksson, H. Nilsson, and F. L. Johansson
   Proceedings of the 14th Spacecraft Charging Technology Conference, Abstract 123, 2016

Reprints were made with permission from the publishers.

Papers not included in the thesis:

- *Spatial distribution of low-energy plasma around comet 67P/CG from Rosetta measurements*
  N. J. T. Edberg, A. I. Eriksson, **E. Odelstad**, P. Henri, J.-P. Lebreton, S. Gasc, M. Rubin, M. André, R. Gill, E. P. G. Johansson, F. Johansson, E. Vigren, J. E. Wahlund, C. M. Carr, E. Cupido, K.-H. Glassmeier, R. Goldstein, C. Koenders, K. Mandt, Z. Nemeth, H. Nilsson, I. Richter, G. Stenberg Wieser, K. Szego and M. Volwerk
  Geophysical Research Letters 42, 4263-4269, 2015

- *Solar wind interaction with comet 67P: impacts of corotating interaction regions*
  N. J. T. Edberg, A. I. Eriksson, **E. Odelstad**, E. Vigren, D. J. Andrews, F. Johansson, J. L. Burch, C. M. Carr, E. Cupido, K.-H. Glassmeier, R. Goldstein, J. S. Halekas, P. Henri, C. Koenders, K. Mandt, P. Mokashi, Z. Nemeth, H. Nilsson, R. Ramstad, I. Richter, G. Stenberg Wieser
  Journal of Geophysical Research 121, 949–965, 2016

- *On the Electron to Neutral Number Density Ratio in the Coma of Comet 67P/Churyumov-Gerasimenko: Guiding Expression and Sources for Deviations*
  E. Vigren1, M. Galand, A. I. Eriksson, N. J. T. Edberg, **E. Odelstad**, S. J. Schwartz
  The Astrophysical Journal 812, 54–63, 2016

Contents

1. Introduction

The subject of this thesis is the evolution and dynamics of the cometary plasma environment of a moderately active Jupiter Family comet before, during and after its closest approach to the Sun. The European Space Agency's Rosetta spacecraft is currently following the comet 67P/Churyumov-Gerasimenko at distances down to ~ 10 km from the nucleus surface, the longest and closest inspection of a comet ever made. Its payload includes a suite of 5 plasma instruments (the Rosetta Plasma Consortium, RPC), providing unprecedented in-situ measurements of the plasma environment in the inner coma of a comet. Two of the plasma instruments, the Ion Composition Analyzer (RPC-ICA) and the Langmuir Probe instrument (RPC-LAP) were provided, and are currently operated, by the Swedish Institute of Space Physics (IRF) in Kiruna and Uppsala, respectively. In this thesis, data from these instruments are used to study the evolution of the cometary plasma environment, primarily by means of the electrostatic potential of the spacecraft, that amounts to a consistent and reliable plasma monitor in the highly variable and dynamic plasma environment in the inner coma.

The thesis is structured as follows: Chapter 2 presents an overview of cometary physics, beginning with a background on the history of cometary science (Section 2.1) and the formation and dynamical evolution of comets (Sections 2.2 and 2.3). This is followed by a review of comet activity and ionization processes (Section 2.4) and the chapter is concluded with an overview of the cometary plasma environment (Section 2.5). Chapter 3 gives a fairly comprehensive review of Langmuir probe measurements in space plasmas, since this is the instrument most used in the studies on which the thesis is based. Chapter 4 provides an introduction to the working principles of relevant particle instruments, since this is the second kind of instrument heavily used in this work. Chapter 5 gives a brief overview of the Rosetta mission and payload and Chapter 6 contains summaries of the two papers included in the thesis.

2. Comets and the cometary plasma environment

2.1 Introduction

The study of comets has long been of great interest to many astronomers. Comets can be very bright and impressive in the night sky and their highly dynamical and seemingly erratic behaviour set them apart from most other celestial objects. Their origin has been the source of some debate over the years. In fact, it is only during the last couple of centuries that it has become clear that they are astronomical in nature, rather than some form of atmospheric phenomena. During the first half of the 19th century, the picture cleared further, showing that the orbits of most comets were much larger than those of the known planets. However, it was still not settled whether their origin could be found within the solar system of if they came from interstellar space.

In 1950, Dutch astronomer J. H. Oort became the one to finally resolve this issue. In his seminal paper (Oort, 1950), he found that the reciprocal semi-major axes $1/a$ of observed comets were strongly biased towards zero, i. e. the parabolic limit. In fact, when plotting the number of observed comets versus reciprocal semi-major axis, he saw a clear spike for $1/a$ between 0 and 10^{-4} AU^{-1}. This became known as the *Oort spike* and indicated that the comets came from very far away, but were still gravitationally bound to the Sun ($1/a > 0$) and so must have their aphelia *inside* the solar system.

Furthermore, Oort found that for most of these near-parabolic comets, the effects of planetary perturbations as they passed through the inner solar system were large enough to place them on clearly different orbits on the way out, either capturing them on more closely bound orbits or ejecting them from the solar system altogether. This led Oort to the conclusion that the comets of the Oort spike must be newcomers to the inner solar system. However, this would require the existence of some source in the outer solar system that could supply the inner solar system with new comets. Since there was no plausible process by which comets could be continuously created in the outer parts of the solar system, Oort inferred the existence of a comet cloud that could act as reservoir of potential newcomers. This cloud has since been known as the *Oort cloud*.

The Oort cloud has been the subject of much research in the past couple of decades. An important issue under investigation has been the mechanism by which comets are injected from the cloud onto orbits with perihelia in the inner solar system (see for example Rickman et al. (2008) and references therein). Another topic has been the prospective existence of an inner cloud

(Hills, 1981), that would not contribute much to the injection of comets into the inner solar system under steady-state conditions, but which may be the source of comet showers observed in geological records (Farley et al., 1998).

Around the same time as Oort formulated his ideas of a distant reservoir of comets, two of his contemporaries, Kenneth Edgeworth and Gerard Kuiper (Edgeworth, 1943; Kuiper, 1951), speculated on the existence of another population of icy bodies, supposedly left-over planet precursors that failed to grow into planets due to the low number density of objects in the outermost regions of the solar nebula. This fitted well with the comet model of Whipple (1950), in which the comets were visualized as having solid nuclei that were conglomerates of ices (e. g. water, carbon dioxide, carbon monoxide, etc.) and meteoric refractory material. For a long time, it was generally believed that this population of objects may have been scattered into the Oort cloud by Neptune and Pluto, but that it did not directly supply the inner solar system with new comets. However, by the end of the 1970s the large number of discovered comets on short-period orbits (< 200 years) with low inclinations proved difficult to explain as a result of injection from the Oort cloud. Fernández (1980) suggested that this subset of comets instead originate from the much closer population of objects postulated by Egdeworth and Kuiper, since known as the *Edgeworth-Kuiper belt*, or simply the *Kuiper belt*. In fact, later studies have shown (Duncan and Levison, 1997) that even this so called *classical* Kuiper belt is insufficient to account for the abundance of observed short period comets, which are now believed to predominantly originate in an extended disk of objects slightly further out, known as the *scattered disk*.

2.2 Formation and dynamical evolution of comets

Several hypotheses have been put forth on how the Oort cloud was formed. The main three alternatives are in-situ formation, interstellar capture and formation in the region of the outer planets followed by outward migration to the present location (Fernandez, 1985). The first two hypotheses have since been more or less discarded; in-situ formation seems unlikely due to the low density of material so far away from the sun and interstellar captures are thought to be very improbable events. Also, the lack of observed comets on hyperbolic trajectories clearly disagrees with the interstellar capture theory. Thus, the third option is the only one that is still seriously considered as a plausible scenario.

Already Oort (1950) suggested that the comets should have formed well inside the planetary system. His view was that they were created as the outer parts of the solar accretion disk condensed into small bodies made up of ices and rocks, i. e. in the same manner as the ice giants (Uranus and Neptune). Those bodies that did not contribute to the formation of these planets were instead scattered outwards into the outer solar system, by planetary and stellar perturbations, where their orbits stabilized out of reach of further planetary

perturbations. This picture has since been improved by including the effects passing stars and the Galactic tide, i. e. the combined gravitational effects of the rest of the galaxy.

Since the time of Oort, several comprehensive simulations of comet migration into the outer solar system using numerical orbit integrations and with the inclusion of passing stars and the Galactic tide effects have been performed (e.g. Duncan et al. (1987), Dones et al. (2004)). In essence, the comets are expected to have formed in the region of the giant planets or beyond, at heliocentric distances of 4-40 AU, since this is where the volatile species typically found in comets, such as H_2O, CO and CO_2 (Bockelee-Morvan et al., 2004), could have survived to be incorporated into planetesimals. Gravitational perturbations by the giant planets, particularly Jupiter and Saturn, would have scattered most of these objects into highly eccentric orbits, with increased semi-major axes but perihelia still in the region of the giant planets. An exception to this are small bodies on near-circular orbits with semi-major axes of about 35 AU or more, out of reach of planetary perturbations. These bodies, that would essentially remain in their original orbits until this day, make up part of the *Kuiper belt* of icy bodies beyond Neptune. Also, Duncan and Levison (1997) showed that some objects with low enough perihelia to experience close encounters with Neptune could get temporarily trapped in mean motion resonances with it, i. e. their orbital periods being related by a ratio of two small integers. Inside these mean motion resonances, various dynamical effects, e. g. the Kozai resonance (Duncan and Levison, 1997), would protect the objects from further close encounters with Neptune and increase their perihelion distances beyond its reach. These bodies, that would survive for the age of the solar system on more eccentric orbits than those of the classical Kuiper Belt, with semi-major axes of $\sim 50 - 500$ AU and perihelia of $30 - 40$ AU, make up the so called *scattered disk* of icy objects beyond the Kuiper Belt.

When comets, whose perihelia are still in the region of the giant planets, obtain semi-major axes on the order of 100 AU or more, their orbital periods become so large that the positions of the perturbing planets at successive perihelion passages are essentially uncorrelated. Therefore, it is possible to model the effects of planetary perturbations on the comets as a random walk of their orbital elements. In fact, Duncan et al. showed that perturbations in perihelion distance q and inclination i are much smaller and less important than the perturbations in reciprocal semi-major axis $1/a$, so that q and i are virtually constant for $a \gtrsim 100$ AU while $1/a$ undergoes a random walk. If the total change in reciprocal semi-major axis $\Delta_{1/a}$ due to perturbations during any single perihelion passage is much smaller than the reciprocal semi-major axis $1/a$ itself, this random walk translates into a diffusion process in $1/a$-space that accelerates with increasing semi-major axis (Yabushita, 1980).

When the semi-major axis of a comet becomes very large, the reciprocal semi-major axis $1/a$ can become very small, so small in fact that the rms change per orbit $D(1/a)$ is no longer infinitesimal in comparison. Then the

diffusion approximation of comet migration fails. Furthermore, as the comets travel farther and farther out from the sun and the planets, the perturbations from the Galactic tidal field and passing stars become increasingly important. The main effect of these additional perturbations is to induce changes in the perihelion distances q of the comets, which can therefore no longer be treated as constants.

The influence of the Galactic tide on comet orbits was thoroughly examined by Heisler and Tremaine (1986) in the context of comet injection into the inner solar system. The main effect of the Galactic tidal field is a torque that perturbs the perihelion distance q. The effects of the tidal torque increases with increasing semi-major axis. This increase is faster than that of the aforementioned diffusion process, which dominates for small orbits, so that at some sufficiently large value of a (~ 6000 AU according to Duncan et al.) the tidal torque overtakes the diffusion process. From then on, the comet mainly sees perturbations of its perihelion distance and not so much of its semi-major axis. Heisler and Tremaine also considered the influence of stellar encounters on comet orbits. The general effect of these encounters is a random walk in comet perihelion distance.

In terms of inclination, the simulations by Duncan et al. showed that the initially ecliptic or near-ecliptic orbits of the comets started evolving towards an isotropic distribution at $a \gtrsim 10^3$ AU. They also found a strong correlation between mean inclination and semi-major axis in this regime such that the mean of $\cos i$ decreased close to linearly with $\log a$. The inclination distribution was almost perfectly isotropic for $a \gtrsim 10^4$ AU. This strong dependence on a enforces the idea that it is the galactic tide and stellar encounters that are responsible for the randomization of comet inclinations.

The end result of this migration is the creation of a reservoir of comets in the outer reaches of the solar system, with typical semi-major axes of $10^4 - 10^5$ AU and a nearly isotropic distribution of inclinations, viz. the Oort cloud.

2.3 Comet reservoirs and dynamic families

Observed comets are typically classified as belonging to different dynamical families depending on the characteristics of their orbit. Historically, the main distinction has been between *long-period comets* and *short-period comets*, comprising comets with orbital periods of more than or less than 200 years, respectively. The short period comets were then typically further subdivided into the *Jupiter Family* of comets with orbital periods less than 20 years and *Halley type* comets with orbital periods between 20 and 200 years. An issue with this taxonomy was that many comets moved between Jupiter Family and Halley type many times in their dynamical lifetimes, e. g. due to close encounters with Jupiter (Levison and Duncan, 1997). Thus, a more convenient taxonomy was introduced, based on the so called *Tisserand parameter* with

respect to Jupiter. Basically, since the Sun and Jupiter are the gravitationally dominant bodies in the solar system, the orbital dynamics of comets in the inner solar system can be considered in the framework of the circular three-body problem. Here, the Sun and Jupiter are considered to be in perfectly circular orbits around their common center of mass and are clearly completely unaffected by any gravitational effects of the passing comet. A comet undergoing a close encounter with Jupiter will typically experience large changes to its orbital elements. However, within the confines of the circular three-body problem, the quantity

$$T_J = \frac{a_J}{a} + 2\sqrt{(1-e^2)\frac{a}{a_J}}\cos i \quad , \tag{2.1}$$

where a_J is the semi-major axis of Jupiter, will be conserved conserved. The Tisserand parameter, T_J, thus allows the distinction between new comets and previously identified comets whose orbits have changed due to close encounters with Jupiter. T_J also reflects the level of interaction of a body with Jupiter and is therefore useful for the classification of comets. Those with $T_J > 3$ are effectively decoupled from Jupiter, orbiting either totally inside (*Encke type*) or outside (*Chiron type*) of Jupiter's orbit. Those with $2 < T_J < 3$ are dynamically dominated by Jupiter and can experience low-velocity encounters with that planet. This is the *Jupiter family* of comets (JFCs). They have typical orbital periods of $\sim 5-20$ years and are the most frequently observed comets. All these comets with $T_J > 2$, Encke type, Chiron type and JFCs, are collectively referred to as *ecliptic comets*, since they tend to have quite low inclinations. In this case one needs to distinguish between ecliptic comets and the transneptunian bodies on stable orbits in the Kuiper belt, which technically have $T_J > 2$ but are not generally considered to be comets as long as they remain in their stable orbits. Comets with $T_J < 2$ are called *nearly isotropic* comets and typically have long orbital periods and a close to isotropic distribution of inclinations. This family includes the Halley type comets (HTCs), now defined as nearly isotropic comets with $a < 40$ AU.

The current picture is that nearly isotropic comets originate in the Oort cloud, where gravitational perturbations due to galactic tidal forces and passing stars occasionally place the on orbits passing through the inner solar system (Heisler and Tremaine, 1986; Rickman et al., 2008). The ecliptic comets on the other hand, in particular the Jupiter Family comets (to which Rosetta's target comet 67P/Churyumov-Gerasimenko belongs), is believed to originate in the scattered disk (Duncan and Levison, 1997), being injected into the inner solar system by successive encounters with the giant planets (Duncan et al., 2004). Thus, it is interesting to note that it is generally the same forces that created and sculpted the comet reservoirs in the outer solar system that are responsible for the injection of some of them into the inner solar system.

2.4 Activity and ionization

Cometary nuclei consist of a mixture of volatile and refractory materials, as first suggested by Whipple (1950). The volatiles are dominated by H_2O, CO and CO_2 (Bockelee-Morvan et al., 2004) while the refractories mostly consist of silicates and organics (Hanner and Bradley, 2004). While on long-period orbits in the outer parts of the solar system, the volatiles remain frozen in the form of ices, but for comets that have been injected into the inner solar system the increased insolation brings about sublimation of the near-surface volatiles. The sublimating gas expands into the surrounding space and forms a coma enveloping the comet nucleus.

2.4.1 The sublimation process

Sublimation is the phase transition of a substance from solid to gas form without passing through the liquid state. Microscopically, it is the process by which atoms or molecules, by virtue of their thermal energy, leave the solid and become free particles. The reverse of this process, when free particles in a gas hit the surface of a solid and attach to it, is called *condensation*.

For a gas in thermal equilibrium with a solid, there exists some pressure p_s at which the rate of condensation on the surface is equal to the rate of sublimation. This is called the *saturation pressure* and it is exponentially dependent on the temperature T of the solid-gas system. Sublimation is an internal process of the solid and it is not affected by the state of the surrounding gas. Thus, the sublimation at a given temperature will be the same irrespective of the gas pressure. However, since the saturation pressure of a gas is readily measurable in a laboratory setting, it is a convenient tool for quantifying the rate of sublimation of a solid material at a given temperature: The sublimation rate, being equal to the condensation rate at saturation pressure, can be calculated from the saturation pressure. In the most simple model, all gas particles are assumed to move with the thermal velocity v_{th}, given by

$$v_{th} = \sqrt{\frac{8k_B T}{\pi m}} \tag{2.2}$$

where k_B is Boltzmann's constant, T is the temperature in Kelvin and m is the particle mass. Equation (2.2) is consistent with the definition of v_{th} as the mean of the magnitude of the velocity of the particles in three dimensions. It can be shown that the corresponding mean of the magnitude of the velocity of the particles in one dimension (i. e. any single direction, for example normal to the solid surface) is equal to $v_{th}/2$. Assuming that half the particles move

towards the surface and the other half away from it and that all particles that hit the surface will stick to it, the sublimation rate can be expressed as

$$Z(T) = n_s \cdot v_{th}/4 = \frac{p_s}{k_B T} \cdot \sqrt{\frac{k_B T}{2\pi m}} = \frac{p_s}{\sqrt{2\pi m k_B T}} \quad , \tag{2.3}$$

where n_s is the particle density in the gas at saturation pressure, given by the ideal gas law as $n_s = p_s/k_B T$.

Neglecting heat conduction into the ice, the heat balance of an illuminated surface can be expressed as

$$P_{\text{absorbed}} - P_{\text{radiated}} - P_{\text{sublimated}} = 0 \quad . \tag{2.4}$$

The absorbed heat comes from the Sun and at Earth's orbital distance the incident solar heat flux is equal to the solar constant F. The incident heat flux scales with the inverse square of the distance to the Sun so that $F(r) = F/r^2$. How much of this heat that is actually absorbed by the body depends on the *bond albedo* A_v of the material (i. e. the fraction of incident light that is reflected or scattered off of the surface) so that

$$P_{\text{absorbed}} = F/r^2 \cdot (1 - A_v). \tag{2.5}$$

The radiated heat is given by

$$P_{\text{radiated}} = \varepsilon \sigma T^4, \tag{2.6}$$

where σ is Stefan-Bolzmann constant and the *emissivity* ε is a measure of how much the radiation properties of the material deviates from a perfect black body ($\varepsilon = 1$).

The sublimated heat is expressed in terms of the *latent heat L*, which is the heat required for the sublimation of a particle from the surface:

$$P_{\text{sublimated}} = L \cdot Z(T). \tag{2.7}$$

Inserting equations (2.5), (2.6) and (2.7) into Equation (2.4) gives

$$\frac{F}{r^2}(1 - A_v) = \varepsilon \sigma T^4 + L \cdot Z(T). \tag{2.8}$$

For ideal gases at low temperatures, the Clausius-Clapeyron relation gives

$$\log p_s = -\frac{L}{R}\left(\frac{1}{T}\right) + c \quad \Rightarrow \quad p_s \propto \exp\left\{-\frac{L}{R}\left(\frac{1}{T}\right)\right\}, \tag{2.9}$$

where R is the specific gas constant and c is a constant. Typical values of L/R for cometary volatiles are on the order of a few thousand Kelvin and the proportionality constant $\exp\{c\}$ is on the order of 10^{10} Nm^{-2} (Prialnik et al., 2004), while $\varepsilon\sigma$ in Equation (2.8) is on the order 10^{-8} Wm^{-2}K^4. Thus, the sublimation term varies much more rapidly with T than the radiation term.

Hence, the sublimation term in Equation (2.8) dominates completely for high temperatures and the radiation term for low temperatures. This means that the temperature of an illuminated body varies with the *inverse of the square root* of the distance to the sun, $T \propto \sqrt{1/r}$, far out in the solar system where the radiation loss is dominant. Near the sun, the sublimation loss dominates and the temperature varies roughly proportionally to the incident solar energy flux, $T \propto r^{-2}$. Hence, at large temperatures close to the Sun the sublimation loss effectively cools the illuminated body and the temperature it obtains depends mostly on the sublimation properties of the material of which it is made up.

In the specific example of comets, the distance from the Sun at which sublimation becomes significant is an important property since it determines where the comet becomes active and can be observed from Earth. For water ice this distance is on the order of 2 - 3 AU. Other substances, such as carbon dioxide and carbon monoxide that have higher saturation pressures at given temperatures, will become active further out. Refractory substances such as minerals have very low saturation pressures and may not become active at all, unless their perihelion is very close to the Sun.

As mentioned above, Equation (2.8) is based on a rather simple model. In a real situation it is often necessary to introduce a *sublimation coefficient* of value less than one in the sublimation term, to account for the fact that not all impacting particles stick to the surface. Also, when sublimation rates are very high, inter-particle collisions may create a backflux of particles towards the surface, reducing the effective cooling and increasing the temperature and sublimation rate of the surface.

2.4.2 Ionization process

The gas of the cometary coma is subject to three main ionization processes: photoionization by solar EUV, electron impact ionization by supra-thermal electrons in the solar wind or the photoelectrons resulting from photoionization, and charge exchange processes with ions in the the solar wind. The probability of an ionization reaction occurring is typically quantified in terms of the *cross section*, σ, for the process, which is the ratio of ions produced per exposed neutral particle to the incident flux I of ionizing radiation or particles. The cross section for a given reaction typically varies with the energy of the incident ionizing particle and the species of the neutral target. For each incident energy and target species, there are generally multiple possible reactions, giving rise to different ion species. For example, the production rate of ions of species j due to photoionization is given by summing over all target species k, of density n_k, the integral over of the product of partial cross sections σ_k^j and I over all incident photon wavelengths λ,

$$P_{j,\text{ph}} = \sum_k n_k \int \sigma_k^j(\lambda) I(\lambda) d\lambda \quad . \tag{2.10}$$

In the case of photoionization, if the coma is not optically thin, the intensity $I(\lambda)$ will decrease exponentially with optical depth τ, which depends on the radial distance from the nucleus as well as the densities and absorption cross sections of the various coma species. More on optical depth can be found in Schunk and Nagy (2009), along with photoionization and absorption cross sections for the relevant species. An important property of photoionization is that, due to conservation of momentum, nearly all the ionization energy gets imparted to the electrons rather than the much heavier ions. Thus photoionization tends to produce rather warm electrons ($\sim 10-15$ eV) wheres the produced ions typically remain at the same temperature as the neutral gas.

Electron impact ionization can be treated in a similar manner, replacing the photon flux by the supra-thermal electron flux. Some relevant cross sections for water can be found in Itikawa and Mason (2005).

Charge exchange processes in the form of electron transfer from neutral coma molecules to solar wind ions may also contribute to the ionization in of the coma gas. There are two main processes: a neutral water molecule in the coma may transfer one of its electrons to a solar wind major ion, H^+, producing a neutral hydrogen atom and an H_2O $^+$ ion, or a cometary neutral (not necessarily water) may transfer one of its electrons to a solar wind minor ion in a high charge state (e.g. O^{5+}, O^{6+}, C^{5+}, C^{6+}, N^{7+}). The latter process generally results in an ion in an excited state and for large enough initial charge states, the de-excitation results in the emission of X-rays that can be observed from Earth, thus providing a means of studying the cometary plasma environment by remote sensing (Lisse et al., 2004).

An important property of the charge exchange process between cometary H_2O molecules and solar wind H^+ ions is that the resulting neutral hydrogen keeps most of the energy that the fast solar wind H^+ ion had, while the H_2O^+ ion added to the plasma remains about as slow as the its parent H_2O molecule. Thus, this charge exchange process effectively cools the plasma.

2.5 Morphology of the cometary plasma environment

2.5.1 Introduction

The cometary plasma environment is sculpted by the interaction between newly formed cometary ions and the flowing plasma of the solar wind. In fact, it was in order to explain the pointing direction of cometary tails that the existence of the solar wind and the interplanetary magnetic field was first deduced (Biermann, 1951; Alfven, 1957). The main body of knowledge presently available on the cometary plasma environment derives from the spacecraft encounters with Comets 1P/Halley, 21P/Giacobini-Zinner and 26P/Grigg-Skjellerup in the 1980s and early 1990s. The picture obtained from the encounter with the highly active Halley has become something of a standard template for the cometary plasma environment, that has so far fit quite well also to less active

comets like Grigg-Skjellerup, at least in terms of the main features. In this Section an overview of this picture is presented in order to provide context and background for the Rosetta results. It is important to note that, in addition to its target being a much weaker comet that Halley, Rosetta will be *much* closer to it than any previous mission, frequently within a few tens of kilometers compared a minimum distance of 600 km of the Giotto spacecraft at Halley. Thus, deviations from the Halley case are expected, and will be briefly pointed out when appropriate. The presentation is built around the graphical illustration of the cometary plasma environment of an active comet shown in Figure 2.1, originally published by Mendis (1988).

2.5.2 Ion pickup by the solar wind

An important process driving much of the dynamics in the cometary plasma environment is the pick-up of newly cometary ions by the solar wind convective electric field. Consider an ion of mass m and charge q created in the solar wind. In the comet reference frame, the solar wind is a flowing plasma with velocity $\mathbf{v}_{sw}$ and permeated by the interplanetary magnetic field $\mathbf{B}_{IMF}$. An ion of velocity $\mathbf{v}_i$ will be accelerated by a convective electric field $\mathbf{E} = -(\mathbf{v}_{sw} - \mathbf{v}_i) \times \mathbf{B}_{IMF}$:

$$\frac{d\mathbf{v}_i}{dt} = \frac{q}{m}(\underbrace{\mathbf{E}}_{-(\mathbf{v}_{sw}-\mathbf{v}_i)\times\mathbf{B}_{IMF}} + \mathbf{v}_i \times \mathbf{B}_{IMF}) = \frac{q}{m}(2\mathbf{v}_i \times \mathbf{B}_{IMF} - \mathbf{v}_{sw} \times \mathbf{B}_{IMF}) \quad (2.11)$$

For simplicity, assume $\mathbf{B}_{IMF} \perp \mathbf{v}_{sw}$ and let $\mathbf{v}_{sw} = v_{sw}\hat{\mathbf{x}}$ and $\mathbf{B}_{IMF} = B\hat{\mathbf{z}}$. Neglecting ion motion parallel to the magnetic field, we have for the x and y components of $\mathbf{v}_i$, v_x and v_y,

$$\dot{v}_x - 2\omega_c v_y = 0 \quad (2.12)$$
$$\dot{v}_y + 2\omega_c v_x = \omega_c v_{sw} \quad , \quad (2.13)$$

where $\omega_c = \frac{qB}{m}$ is the ion cyclotron frequency and the dot notation is short hand for $\frac{d}{dt}$. Differentiating Equation (2.12), solving for $\dot{v}_y$ and substituting the result for $\dot{v}_y$ in Equation (2.13) gives

$$\dot{v}_y = \frac{\ddot{v}_x}{2\omega_c} \quad (2.14)$$
$$\ddot{v}_x + 4\omega_c^2 v_x = 2\omega_c^2 v_{sw} \quad . \quad (2.15)$$

Equation (2.15) is a non-homogeneous, linear, second order differential equation, the general solution to which is the sum of the general solution to the
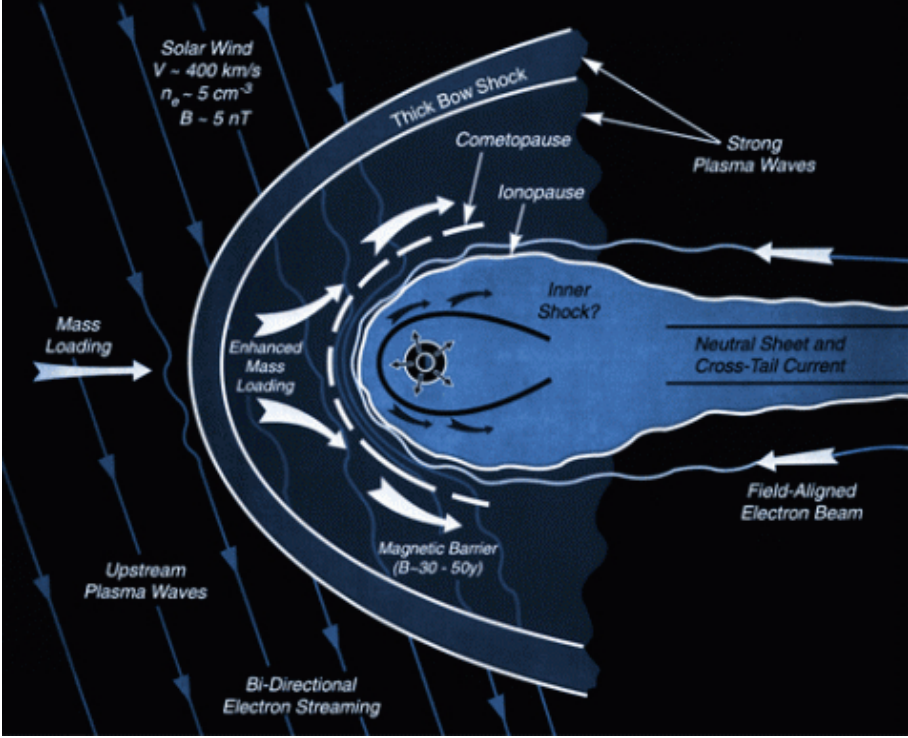
Figure 2.1. Plasma environment of an active comet nucleus. *(Image credit: NASA/JPL)*

corresponding homogenous equation ($v_{x,h}$) and a particular solution to the non-homogenous equation ($v_{x,p}$):

$$v_x = \underbrace{C\cos 2\omega_c t + D\sin 2\omega_c t + Et + F}_{v_{x,h}} + \underbrace{\frac{1}{2}v_{sw}}_{v_{x,p}} \quad , \tag{2.16}$$

where C, D, E and F are arbitrary constants. The initial speed of the newly created ion, being of the same order of magnitude as the outflow speed of the neutral gas (~ 1 km/s), is entirely negligible compared to typical solar wind speeds (~ 400 km/s), so the ion may be considered to be initially at rest. Given that the solar wind electric field is in the $\hat{\mathbf{y}}$ direction and the Lorentz force vanishes for a particle at rest, the initial acceleration of the ion will be zero in the $\hat{\mathbf{x}}$ direction. Imposing such initial conditions on Equation (2.16) gives $D = E = 0$ and $F = -(C + \frac{v_{sw}}{2})$. Equation (2.14) now gives

$$\dot{v}_y = -2\omega_c C\cos 2\omega_c t \quad , \tag{2.17}$$

but we know that the initial acceleration in the $\hat{\mathbf{y}}$ direction is $-\omega_c v_{sw}$, thus we have $C = v_{sw}$ and the ion motion becomes

$$v_x = v_{sw}(1 + \cos 2\omega_c t) \qquad (2.18)$$
$$v_y = -v_{sw} \sin 2\omega_c t \quad . \qquad (2.19)$$

Defining the origin as the starting point of the ion, integration of Equations (2.18) and (2.19) yields

$$x(t) = v_{sw}t + \frac{v_{sw}}{2\omega_c} \sin 2\omega_c t \qquad (2.20)$$
$$y(t) = \frac{v_{sw}}{2\omega_c} \cos 2\omega_c t \quad . \qquad (2.21)$$

The ion thus follows a cycloid motion at twice the cyclotron frequency, with an effective drift velocity of v_{sw} in the solar wind direction. Such an ion is said to have been *picked up* by the solar wind and is referred to as a *pick-up ion*. In fact, since the interplanetary magnetic field is frozen in to the solar wind,

$$\mathbf{E} + \mathbf{v}_{sw} \times \mathbf{B}_{IMF} = 0 \qquad (2.22)$$

in the comet reference frame. Taking the vector product of Equation (2.22) with B_{IMF} from the right and recalling that $\mathbf{B}_{IMF} \perp \mathbf{v}_{sw}$, $\mathbf{v}_{sw}$ can be solved for, giving

$$\mathbf{v}_{sw} = \frac{\mathbf{E} \times \mathbf{B}_{IMF}}{B_{IMF}^2} \quad , \qquad (2.23)$$

where B_{IMF} is the magnitude of $\mathbf{B}_{IMF}$. Equation (2.23) is the well-known expression for $\mathbf{E} \times \mathbf{B}$ drift of a plasma in the presence of an electric field parallel to the background magnetic field. Thus, the phenomenon of ion pick-up can be viewed in the cometary reference frame as $\mathbf{E} \times \mathbf{B}$ drift of the cometary ions in the convective electric field of the solar wind.

This pick-up process described above may be complicated in the case of a strongly non-homogeneous ion density. It should hold locally where the ion gyro-radius is sufficiently larger than the gradient scale of the ion density. The latter cannot be longer than the distance to the nucleus, so in practice the possible applicability of (2.27) will be restricted to distances from the nucleus several times the gyro-radius of a pick-up ion. For typical solar wind parameters of 400 km/s and 1 nT, this means several hundred thousand km. Effects of mass loading and magnetic field compression can decrease this value, but for Rosetta, staying within a few thousand km of the nucleus since arrival and most of the time within a few 100 km, we clearly do not expect to observe an environment dominated by fully picked up cometary ions (Nilsson et al., 2015a).

The pick-up ion population, being continuously replenished by newly created ions in different phases of their gyro-motion, forms a ring distribution

in phase space. If the magnetic field is not exactly perpendicular to the solar wind velocity, no convective electric field exists in the direction of the component of the solar wind velocity parallel to **B**. Hence the ions will not be immediately accelerated in this direction, thereby forming an ion beam in the solar wind frame. Thus, the general phase space configuration of the pick-up ions in the solar wind frame is that of a combined ring-beam distribution. This distribution is highly unstable to a number of different low-frequency wave modes, perhaps the most important one being ion cyclotron waves (Tsurutani, 1991). No sign of such waves has yet been discovered in the Rosetta data.

2.5.3 Mass loading of the solar wind

The pick-up process described in the previous section clearly imparts momentum to the initially stationary cometary ions. Conservation of momentum requires that this come from somewhere; in fact, an equal amount of momentum is removed from the solar wind, causing it to decelerate. The continual influx of non-decelerated solar wind plasma from upstream of the ion pick-up region leads to a compression and densification of the decelerating plasma, a process known as *mass loading*. In the previous section, such feedback on the solar wind from the pick-up ions was neglected, assuming that the solar wind conditions remain unchanged throughout the ion pick-up process. While this may be valid in the limit of small densities of cometary ions, it certainly does not hold once this density becomes appreciable compared to the solar wind. Indeed, most of the large scale processes in the plasma environment of an active comet derive in one way or another from the mass loading process.

The physical mechanisms responsible for the momentum transfer are rather complicated when examined in detail (Coates and Jones, 2009). However, a simplified macroscopic model can be obtained on temporal and spacial scales relevant for the ion dynamics (Omidi et al., 1986). Then, the much lighter and more mobile electrons essentially behave as a massless fluid that immediately moves to cancel out any electrostatic fields in the plasma. Neglecting resistive effects, any currents in the plasma will also be canceled out by electron motions. Charge neutrality and the zero-current condition then give (in the comet reference frame where $\mathbf{v}_i = 0$ to begin with)

$$
\begin{aligned}
\rho_e &= n_{sw} + n_i - n_e = 0 & (2.24) \\
\mathbf{J} &= n_{sw}\mathbf{v}_{sw} - n_e\mathbf{v}_e = 0 \quad , & (2.25)
\end{aligned}
$$

where n_{sw} and $\mathbf{v}_{sw}$ are the density and velocity of the undisturbed solar wind, respectively, n_i and v_i the density and velocity of the pick-up ions, and n_e and $\mathbf{v}_e$ are the density and velocity of the electrons, modeled here as a single fluid since their massless nature means that they will be instantly picked up

and mixed into the combined flow. The equation of motion of the massless electrons ($m_e = 0$) is

$$m_e \frac{d\mathbf{v}_e}{dt} = -e(\mathbf{E} + \mathbf{v}_e \times \mathbf{B}_{\text{IMF}}) = 0 \quad , \tag{2.26}$$

while solving Equations (2.24) and (2.25) for $\mathbf{v}_e$ gives

$$\mathbf{v}_e = \frac{n_{sw}\mathbf{v}_{sw}}{n_{sw} + n_i} \quad . \tag{2.27}$$

Thus, the pick-up process will decrease the bulk electron velocity by a factor $n_{sw}/(n_{sw} + n_i)$. The resulting electric field can be obtained by solving for $\mathbf{E}$ in Equation (2.26) and substituting Equation (2.27) for $\mathbf{v}_e$, giving

$$\mathbf{E} = \frac{n_{sw}}{n_{sw} + n_i}\mathbf{v}_{sw} \times \mathbf{B}_{\text{IMF}} \quad . \tag{2.28}$$

The $\mathbf{E} \times \mathbf{B}$ drift velocity of the pick-up ions is then

$$\mathbf{v}_{i,\text{final}} = \frac{1}{B_{\text{IMF}}^2} \frac{n_{sw}}{n_{sw} + n_i}(\mathbf{v}_{sw} \times \mathbf{B}_{\text{IMF}}) \times \mathbf{B} = \frac{n_{sw}\mathbf{v}_{sw}}{n_{sw} + n_i} = \mathbf{v}_e \tag{2.29}$$

and the same holds for the original solar wind ions. Hence, the result of the mass loading is a combined flow of solar wind ions, pick ions and electrons at a reduced speed given by Equation (2.27).

2.5.4 Bow shock formation

The solar wind constitutes a *supersonic* flow of plasma, in the sense that the bulk (or drift) speed is higher than the speed of the constituent particles in their gyrating orbits. For an active comet, the deceleration of the solar wind due to the mass loading process described in the previous section can be strong enough to induce a transition to subsonic flow. This transition gives rise to a *bow shock*, where the the mass-loaded solar wind is abruptly slowed, heated, compressed, and diverted. Due to the tenuous nature of the solar wind, the mean free path of two-body Coulomb collisions is too large for them to affect the formation or energy dissipation of the shock. The cometary bow shock is therefore a collision-less shock, where the dynamics is dominated by wave-particle interactions driven by the instabilities that arise from particles having similar bulk and gyration speeds.

Cometary bow shocks are different from the bow shocks of magnetized bodies like the Earth in that the mass loading takes place on much larger spatial scales than the solar wind-magnetosphere interaction. At Earth, the bow shock distance can be estimated from the balance of the solar wind ram pressure against the magnetic pressure of Earth's dipole at the magnetopause.

At a comet, such a simple treatment is not possible. Instead, analytical one-dimensional fluid models by Biermann et al. (1967) and Flammer and Mendis (1991) showed that the bow shock would occur at a distance where the mass flux density, which increases as a consequence of mass loading, reaches a critical value which depends on the ratio of specific heats, the dynamic pressure, the magnetic pressure and the thermal pressure in the undisturbed solar wind. Actual stand-off distances can range from $\sim 10^3$ km for weakly outgassing comets (Koenders et al., 2013) to $\sim 10^5$ km (Coates, 1995) for very active comets.

No bow shock has been identified in the Rosetta data, most likely because of the close distance to the nucleus during the time when the activity was sufficient for a bow shock to form.

2.5.5 Cometopause and collisionopause

Downstream of the bow shock, the mass loading continues at an accelerated rate as the density of cometary ions increases towards the nucleus. The increased densities of cometary neutrals and ions also mean that collisions become more and more frequent with decreasing cometocentric distance. The distance at which collisions first become important for the plasma dynamics is referred to as the *collisionopause*. A more quantitative formulation of this can be obtained by comparing the residence time of the plasma in the region of interest, the *characteristic transport time* τ_T, to the characteristic collision time τ_c. τ_T is typically taken to be the ratio of the cometocentric distance and local flow speed, while τ_c is the average time between collisions. The collisionopause is the location where $\tau_T \approx \tau_c$. It is important to note that there are many different kinds of collisional processes occurring in the cometary coma, each with its own characteristic time τ_c and therefore also its own separate collisionopause. Examples of collisional processes in the coma include charge exchange, electron cooling and ion-neutral chemistry. The collisionopause for charge-exchange between solar wind protons and neutrals, described in Section 2.4.2, is often called the *cometopause* (Cravens, 1991), because it produces a transition (sometimes quite sharp, sometimes rather broad) of the plasma composition from solar wind dominated to cometary dominated.

2.5.6 Flow stagnation and magnetic barrier

Inside the cometopause, the solar wind is subject to strong deceleration due to collisions of solar wind ions with cometary neutral molecules. It also cools by charge exchange reactions (c. f. 2.4.2) between solar wind ions, or energetic pick-up ions created upstream, and the cold cometary neutrals. For very active comets, with vast solar wind interaction regions where spatial scales are large, the typical gradient length in the plasma is much greater than the

ion gyro-radius. Then, the magnetic field is frozen into the solar wind and effectively piles up in front of the comet nucleus as the solar wind decelerates and compresses. Thus, in this region, known as the *magnetic barrier region*, the field strength increases and the magnetic pressure grows, at the expense of solar wind dynamic pressure. As a result, the solar wind eventually almost completely stagnates.

2.5.7 Magnetic field line draping

The un-impeded solar wind to the sides of the of the cometopause drags the field lines along downstream, causing them to wrap around the comet, a phenomenon known as *magnetic field line draping*. Downstream, towards the tail of the comet, the magnetic field thus tends to form two adjacent regions of oppositely directed field lines. The resulting curl of the magnetic field is accompanied by a cross-tail current perpendicular to the magnetic field lines in a thin layer between the regions of oppositely directed magnetic field. At the center of this layer, the magnetic field essentially cancels out in a thin sheet called the *neutral sheet*.

The continuous flow of solar wind from upstream brings an influx of energy to the piled-up and draped magnetic field. As the fields build up around the comet, the field lines release some of this magnetic energy by slipping around the comet and rejoining the solar wind downstream. If this mechanism fails to dispel enough energy, e. g. in the case of impacting CMEs or other strong external perturbations to the system, the oppositely directed field lines in the tail may undergo magnetic reconnection, giving rise to a *tail disconnection* event. In this kind of event, a part of the tail breaks off and is accelerated downstream. Also, beams of electrons may shoot back along the field lines into the region of the inner coma, in the form of so-called *field-aligned electron beams*.

2.5.8 Ionopause and diamagnetic cavity

The draped and piled-up magnetic field at the inner edge of the magnetic barrier eventually builds up enough magnetic pressure so that the total $\mathbf{j} \times \mathbf{B}$ force balances the drag force of of the outflowing neutral gas on the stagnant cometary ions. Here, a tangential discontinuity forms, that separates the mass-loaded solar wind plasma from the purely cometary plasma inside of the discontinuity. This constitutes a compositional boundary generally called the cometary *ionopause*. In fact, if the magnetic field is frozen-in to the mass-loaded solar wind ions, it will not be able to penetrate inside this boundary either. Thus, a so called *diamagnetic cavity* forms inside the cometary ionopause within which the magnetic field vanishes.

2.5.9 Inner shock

Because of the effective cooling of ions due to collisions with neutrals in the dense innermost part of the coma, inside the diamagnetic cavity, the ion thermal speed is low and the flow will be supersonic close to the nucleus. However, the plasma will clearly be subsonic at the stagnation point just outside of the cometary ionopause. Therefore, an *inner shock*, analogous to the bow shock discussed in Section 2.5.4, is expected to form somewhere inside the ionopause, where the transition from supersonic to subsonic flow occurs. The existence and nature of this shock remains unclear. Goldstein et al. (1989) observed a thin density spike at the inner edge of the ionopause of comet 1P/Halley where recombination was the primary loss mechanism limiting the maximum density and it has been suggested (Cravens, 1989) that this so called *recombination layer* could fill the function of an inner shock, but this is far from being generally accepted.

No clear evidence of an inner shock has been so far been found in the Rosetta data.

2.6 First results from Rosetta at comet 67P

To provide context and background for the papers of this thesis, here follows a brief review of other work describing the main constituents of, and features in, the plasma environment of Rosetta at comet 67P during the first months of the mission.

2.6.1 Ions

The first cometary plasma to be detected was cometary pick-up ions at a distance of 100 km from the nucleus on August 7, 2014, by RPC-ICA (Nilsson et al., 2015a). These were water ions at nearly 100 eV, created upstream and accelerated towards the spacecraft by the convective electric field perpendicular to the solar wind direction. The first locally produced ions were detected by RPC-IES on August 19, 2014, at a distance of ~ 80 km from the nucleus (Goldstein et al., 2015). These were also seen by ICA from September 21, 2015, at a distance of 28 km, and had typical energies of 5-10 eV, close to the spacecraft potential. It is unclear whether the appearance of these ions in ICA was triggered by their local density increasing above the measurement threshold of the instrument, or if it was because the increasingly negative spacecraft started pulling them in over the instrument energy threshold. Possibly, it is a combination of both effects.

Deflection of the solar wind was also first observed around September 21, 2014, with protons being deflected by about $20°$. The total plasma density was typically on the order of $5-10$ cm^{-3} in September 2014, at ~ 30 km from the

nucleus. This is comparable to the solar wind proton density, but the mass density is about an order of magnitude larger. In addition, detection of He^+ ions showed that charge exchange reactions had begun to occur, since these ions are created by charge exchange between solar wind He^{2+} and cometary water molecules. Thus, the solar wind was already clearly influenced by interaction with the cometary plasma. By late November 2014, the deflection angle of solar wind protons had increased to more than $50°$ at similar cometocentric distances (Behar et al., 2016).

The flux of accelerated cometary water ions increased dramatically between August 2014, at 3.6 AU, and March, 2015, at 2.0 AU, on average by 4 orders of magnitude (Nilsson et al., 2015b). This was observed also further away from the nucleus, during the excursions out to 250 km from the nucleus in February, 2015.

2.6.2 Electrons

The electron temperature was found to be quite high, $\sim 5 - 10$ eV, a consequence of the low collision rate in the tenuous neutral gas of the inner coma. In the presence of substantial fluxes of such warm electrons, the spacecraft charges to negative potentials of up to several tens of volts. In addition to these warm thermal electrons, a supra-thermal electron population, accelerated up to several hundreds of eV, was detected by IES (Clark et al., 2015). Their origin is still unclear, but they appear to become more numerous during periods of stormy solar wind (Edberg et al., 2016), which might indicate that the responsible heating mechanism is connected to the solar wind energy input. There was a general trend of increasing fluxes of this supra-thermal electrons during the first moths of the mission, somewhat resembling the increase in accelerated water ion flux observed by ICA (c. f. Section 2.6.1). The A third population of cold electrons, with characteristic energies of less than 0.1 eV, has recently been identified in the data from RPC-LAP. These are observed very intermittently as pulses typically lasting for a few to a few tens of seconds as seen in the spacecraft frame. They presumably obtain their low temperatures from cooling by collisions with neutrals in the densest inner part of the coma, though the reason behind their sporadic occurrences is still unclear.

2.6.3 Evolution and general features

The tilted rotation and complex geometry of the nucleus (Sierks et al., 2015) produced strong diurnal and seasonal variations in the outgassing, with most of the gas and dust coming from the northern (summer) hemisphere of the nucleus, with the neck region between the two lobes being the most active part (Hässig et al., 2015; Sierks et al., 2015; Gulkis et al., 2015; Bockelée-Morvan

et al., 2015). That came through also in the near-nucleus plasma environment ($\lesssim$ 50 km from the nucleus), where the plasma density (Edberg et al., 2015) and spacecraft potential (Paper I) peaked over the neck region in the northern hemisphere, closely following the neutral density. This indicates that local ionization, in the sense of plasma produced at or inside the cometocentric distance of the spacecraft, was the dominant source of the local plasma.

Edberg et al. (2015) reported densities on the order of 200 cm^{-3} in October 2014, when at 10 km from the nucleus. The total neutral density was found to fall off as $1/r^2$ with distance r from the nucleus (Hässig et al., 2015) while the plasma density decayed as $1/r$, consistent with a locally produced plasma expanding radially at constant speed. However, this interpretation requires the absence of any significant solar wind electric field. Possibly, this field is quenched close to the nucleus by significant ion pickup and mass loading, as indicated by the solar wind deflection observed by ICA.

3. Langmuir probe measurements in space plasmas

3.1 Introduction

This chapter provides an introductory summary of the expressions for the currents to a Langmuir probe in a space plasma and the theory behind them. The focus is on currents due to ambient plasma particles (electrons and ions) and the photoelectron current due to photoemission from a sunlit probe surface. The exposition is based on the presentations of OML theory (Orbit Motion Limited) in chapter 3 of Engwall (2006), chapter 3 of Holmberg (2013) and Laframboise and Parker (1973), and the treatments of photoelectron currents in Grard (1973) and Pedersen (1995).

3.2 OML currents

When an electrical conductor is immersed in a plasma, the thermal motions of charged particles in the plasma will cause some of them to impact on the conductor surface. These impacts give rise to a current, *to* the conductor in the case of positively charged ions and *from* the conductor in the case of electrons. The magnitudes of these currents depend on the density and velocity of the respective particle species near the conductor. Thus, an electrical conductor can be used as a probe to measure the characteristics of a plasma. Quantitively, the current *to* a probe due to a single particle species is given by the product of the particle charge q and the particle flux to the probe Φ

$$I = q\Phi = q \int_{v_n < 0} \oint_S f(\mathbf{r}, \mathbf{v}) \underbrace{\mathbf{v} \cdot \hat{\mathbf{n}}}_{v_n} \, dS \, d^3v \qquad (3.1)$$

where $\hat{\mathbf{n}}$ is the normal to the probe surface and $f(\mathbf{r}, \mathbf{v})$ is the distribution function such that $f(\mathbf{r}, \mathbf{v})d\mathbf{v}$ gives the number of particles per unit volume with velocities between $\mathbf{v}$ and $\mathbf{v} + d\mathbf{v}$ at position $\mathbf{r}$ in the plasma. S is the probe surface and v_n is the component of the particle velocity normal to it. The integration is over negative v_n only, since particles with positive normal velocity will move away from the probe and not impact on its surface.

A straightforward calculation of the probe currents from equation (3.1) requires that the plasma distribution function $f(\mathbf{r}, \mathbf{v})$ be known at the probe surface. This is most often *not* the case since the presence of the probe and

any charge it carries inevitably perturbs the plasma near to it. Specifically, a *charged* probe will give rise to an electric field that attracts plasma particles of opposite charge to the probe and repels particles of like charge. Thus, the plasma particles that pass by the probe will see their trajectories deflected, *towards* the probe in the case of opposite charge and *away* from it in the case of like charge. This creates a density difference between electrons and (positive) ions near the probe, which manifests as a net space charge that partially cancels out the potential field of the probe. The characteristic distance over which the potential is shielded out is known as the *Debye length* λ_D of the plasma (Chen, 1984). Even in the case of an uncharged probe, the surrounding plasma will still be perturbed. This is because some of the particle trajectories will be blocked by the the probe, leading to a change in the velocity distribution of the plasma. The perturbed region near the probe is typically called a *sheath*.

The perturbative effects of a probe on the plasma in which it is immersed are very difficult to treat analytically. Therefore, it is desirable to come up with some other method for calculating the probe currents. This problem was first treated by Mott-Smith and Langmuir in 1926. They used the assumption that sufficiently far from the probe, outside the sheath, the plasma will be unperturbed and thus have a known distribution function (e.g. Maxwellian). If all particles that impact on the probe and contribute to the current originate from the region outside the sheath, then it should be enough to integrate the velocity distribution at the outer edge of the sheath over those regions in velocity space for which particles are able to reach the the probe. The problem is thereby reduced to finding the regions in velocity space at every point on the sheath edge that give rise to trajectories through the sheath that end on the probe. This is illustrated in Figure 3.1 for a spherical probe, where ϕ_0 and ϕ_p are the probe and plasma potentials, respectively, and s is the sheath thickness.

However, the procedure outlined above only constitutes a minuscule simplification since the relevant particle trajectories clearly depend on the detailed properties of the sheath. Mott-Smith and Langmuir solved this problem by simply neglecting all the effects of the plasma. The particle trajectories are then governed solely by the conservation of energy and angular momentum in the vacuum field of the probe. This approximation holds as long as the Debye length, and hence the sheath thickness, is large. The screening effect of the plasma is then weak and has little effect on the motions of particles in the sheath. It is thus possible to calculate the probe currents from simple mechanics, taking the limit of the resulting expressions as the radius of the sheath edge goes to infinity. This approach is called *Orbit Motion Limited (OML)*.

The detailed calculations for a spherical probe in a stationary (non-drifting) plasma are presented in Mott-Smith and Langmuir (1926) and Engwall (2006).
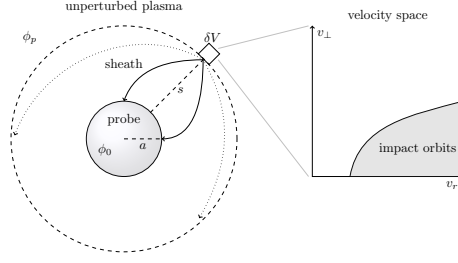
Figure 3.1. Illustration of OML current derivation for a spherical probe.

Defining the probe bias potential with respect to the plasma $U_B = \phi_0 - \phi_p$ and the *normalized potential* (for particle species j)

$$\chi_j = \frac{q_j U_B}{k_B T_j},$$ (3.2)

the result can be written

$$I_j = \begin{cases} I_{j0}(1 - \chi_j), & \chi_j \leq 0 \\ I_{j0}\exp\{-\chi_j\}, & \chi_j \geq 0 \end{cases}$$ (3.3)

where the *random current* I_{j0} is given by

$$I_{j0} = -4\pi a^2 n_j q_j \sqrt{\frac{k_B T_j}{2\pi m_j}}.$$ (3.4)

I_{j0} is the current that would flow *from* an unbiased probe, that is when $U_B = 0$ (or, equivalently, $\phi_0 = \phi_p$). In equations (3.2)-(3.4), q_j, T_j, n_j and m_j are the charge, temperature, number density and mass of particle species j, respectively.

   Equation (3.4) shows that I_{j0} is proportional to the surface area $4\pi a^2$ of the probe. It is interesting to note that this is the only way by which the probe size affects the current. This means that the probe current can just as well be expressed in terms of current density and probe area. In fact, Equation (3.3) also holds for the current density, if I_{j0} is replaced by the *random current density* given by

$$J_{j0} = -n_j q_j \sqrt{\frac{k_B T_j}{2\pi m_j}}.$$ (3.5)

This representation is convenient when comparing the current collecting properties of different probe geometries.

   A schematic plot of Equation (3.3) for the current density is shown in Figure 3.2, which also includes the corresponding curve for an infinite[1] planar surface. The planar geometry is instructive because, for attractive potentials

---

[1]*Infinite* here refers to a plane large enough that edge effects can be neglected.
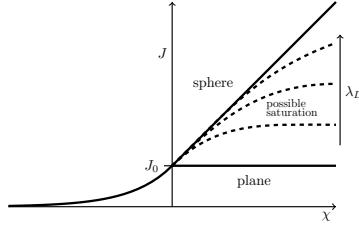
Figure 3.2. Schematic of the OML current-voltage relationships for a spherical probe and a semi-infinite planar surface.

$\chi_j \geq 0$, all particles that enter the sheath will reach the probe. Thus, the current to the probe will be equal to the random thermal current to the sheath. In planar geometry, the total area of the sheath edge is equal to the surface area of the probe so the probe current density is just the random thermal current density J_0. This actually holds for a probe of any shape in the limit as the sheath thickness goes to zero. This *thin sheath limit* is only applicable for very dense plasmas that can be found in laboratory settings. However, an analogous phenomenon can occur for a spherical probe in a dense space plasma if the bias potential is very large. All particles inside the sheath are then collected by the probe and the current saturates to a constant value instead of increasing linearly with the potential as prescribed by Equation (3.3).

So far, only non-drifting plasmas have been considered. However, in space there is often a relative drift velocity v_D between the spacecraft and the plasma. The OML formulas for a probe in a drifting Maxwellian plasma are derived by Medicus (1961) and Engwall (2006) for a spherical probe. In Høymork (2000) they are expressed in a slightly more convenient form in terms of the *error function*

$$\text{erf}(x) = \frac{2}{\sqrt{\pi}} \int_0^x \exp\left\{-t^2\right\} dt, \tag{3.6}$$

giving

$$I_j = \frac{I_{j0}}{2} \left[\sqrt{\pi} \left(S + \frac{1}{2S} - \frac{\chi_j}{S} \right) \text{erf}(S) + \exp\left\{-S^2\right\} \right] \tag{3.7}$$

for $\chi_j \leq 0$ (attractive potentials) and

$$I_j = \frac{I_{j0}}{4S} \left[\sqrt{\pi} \left(S^2 + \frac{1}{2} - \chi_j \right) \left(\text{erf}\left(S + \sqrt{\chi_j}\right) - \right.\right.$$
$$\left. \text{erf}\left(\sqrt{\chi_j} - S\right) \right) + \left(S - \sqrt{\chi_j}\right) \exp\left\{-\left(S + \sqrt{\chi_j}\right)^2\right\}$$
$$\left. + \left(S + \sqrt{\chi_j}\right) \exp\left\{-\left(\sqrt{\chi_j} - S\right)^2\right\} \right] \tag{3.8}$$

for $\chi_j \geq 0$ (repulsive potentials), where

$$S = \frac{v_D}{\sqrt{\dfrac{2k_B T_j}{m_j}}} = \frac{v_D}{v_{\text{th}}} \tag{3.9}$$

and v_D is the drift velocity of the plasma. v_{th} is the *thermal velocity*, defined here as the speed of a particle with energy $k_B T$ or, equivalently, the most probable speed of a particle obeying a Maxwellian distribution with temperature T.

Equations (3.7) and (3.8) can be greatly simplified for large speed ratios, $v_D \gg v_{\text{th}}$. Then $S \gg 1$ and the exponentials vanish. Furthermore, the error function tends to unity for large positive arguments (and to -1 for large negative arguments) so both Equations (3.7) and (3.8) reduce to

$$I_j = I_{j0} \cdot \frac{\sqrt{\pi}}{2} S \left(1 + \frac{1}{2S^2} - \frac{\chi_j}{S^2}\right), \tag{3.10}$$

which has the very simple form of a straight line in the current-voltage diagram of the probe. If the speed ratio becomes so large that also the $1/S^2$ terms are negligible, Equation (3.10) reduces to

$$I_j = I_{j0} \cdot \frac{\sqrt{\pi}}{2} S = \pi a^2 n e v_D = I_{\text{ram}}, \tag{3.11}$$

where Equations (3.4) and (3.9) were used for the second equality. This is just the ram current to the probe.

3.3 Photoelectron current

When an electrical conductor is exposed to sunlight, electrons may be knocked out of the material by impacting photons in a process known as *photoemission*. If some of the emitted electrons have enough energy to overcome the potential barrier around the conductor they will form an outward electron flux, which manifests as an electrical current *to* the conductor. This current is called a *photoelectron current* and it can have a big influence on the current-voltage characteristics of a sunlit probe in a space plasma.

The photoemission of a conductive surface in space depends on properties of the material and the solar spectrum. Quantitatively, the photoelectron flux Φ_e from the surface is given by

$$\Phi_e = \int_0^\infty \Phi_{\text{ph}}(w) Y(w) dw, \tag{3.12}$$

where $\Phi_{\text{ph}}(w)$ is the incident flux of photons with energies between w and $w + dw$. $Y(w)$ is the *photoelectron yield* of the material, i. e. the (average)

number of photoelectrons emitted per incoming photon of energy w. These quantities usually have to be determined empirically. Grard (1973) uses laboratory measurements of the photoelectron yield and in situ measurements of the solar photon flux in space (at Earth's orbital radius) to calculate predictions of the photoemission from a number of different materials.

The incident photon flux Φ_{ph} clearly depends on the angle of the illuminated surface to the sun. For a non-planar probe this typically varies over the probe surface, which implies that the photoemission is be non-uniform. However, if the photoelectron *yield* is uniform the total rate of photoemission from the probe depends only on the total number of incoming photons. Since this is given by the product of the probe's projected area to the Sun A_p and the total solar photon flux at the probe, it is possible to define an *average photoelectron flux* $\bar{\Phi}_e$ such that the total rate of photoemission from the probe is given by $\bar{\Phi}_e \cdot A_p$. In the case of a planar surface under normal incidence, $\Phi_e = \bar{\Phi}_e$.

If a probe is at a negative potential with respect to the plasma, all the photoelectrons emitted from its surface escape and the photoelectron current saturates. The resulting *photoelectron saturation current* $I_{ph,0}$ is given by

$$I_{ph,0} = J_{ph,0} \cdot A_p \tag{3.13}$$

where $J_{ph,0}$ is the *saturation current density*, simply given by the average photoelectron flux from the surface multiplied by the electron charge[2]:

$$J_{ph,0} = -e \cdot \bar{\Phi}_e. \tag{3.14}$$

For a positively charged probe the situation is more complicated. Only photoelectrons with sufficient kinetic energy to escape the potential well of the probe will contribute to the current. Thus, the photoelectron current in this case depends on the energy distribution of the photoelectrons. In terms of the *normalized* distribution $p(\psi)$, where ψ is the photoelectron energy, the current can be expressed as

$$I_{ph} = I_{ph,0} \int_{U_B}^{\infty} p(\psi) d\psi. \tag{3.15}$$

It now remains to find $p(\psi)$. Again, empirical data has to be invoked, showing that the photoelectron distribution is nearly Maxwellian with a temperature on the order of 1.5 eV (Grard, 1973). Remarkably, this appears to hold for all the different materials investigated by Grard and is therefore often taken to be generally applicable to any material. With the assumption of Maxwellian photoelectrons the photoelectron current to a positively charged probe can be

---

[2]$J_{ph,0}$ is not a *physical* current density, but rather an *effective* current density that relates the total photoelectron saturation current of a probe to its effective photon collecting area.

obtained from Equation (3.15). The detailed calculations are performed by Grard (1973). The result is

$$I_{\text{ph}} = I_{\text{ph},0} \left(1 + \frac{eU_B}{k_B T_{\text{ph}}}\right) \exp\left\{-\frac{eU_B}{k_B T_{\text{ph}}}\right\}. \tag{3.16}$$

It is important to note that Equations (3.15) and (3.16) are strictly valid only when the probe is small enough (relative to the Debye length[3]) so that it can be approximated by a point source. Then the photoelectrons are emitted radially out of the probe and all of the kinetic energy goes into motion perpendicular to the equipotential surfaces, as shown in Figure 3.3(a). Otherwise the photoelectron energy ψ in Equation (3.15) may be partly due to motion *parallel* to the equipotential surfaces, that does not contribute to overcoming the potential barrier. The most extreme example of this is that of an infinite planar surface. The energy ψ in Equation (3.15) must then be replaced by the *perpendicular* kinetic energy $\psi_\perp$. Fortunately, the energy distribution associated with perpendicular motion can in this case be related to the total energy distribution, which was assumed to be Maxwellian, so the resulting expression for the photoelectron current can be calculated without any further assumptions (Grard, 1973). The result is

$$I_{\text{ph}} = I_{\text{ph},0} \exp\left\{-\frac{eU_B}{k_B T_{\text{ph}}}\right\}. \tag{3.17}$$

Equations (3.16) and (3.17) are plotted schematically in Figure 3.4. Which one of these expressions that is appropriate to use in a given situation is not always clear, but they are expected to provide good upper and lower limits for the photoelectron currents that can be obtained by probes of different sizes and geometries[4].

Unfortunately, the laboratory measurements of the photoelectron yield used by Grard have shown some severe deficiencies as predictors of the photoemission characteristics of the respective materials in space. Pedersen (1995) reported that the photoelectron saturation currents for the vitreous carbon probes on the GEOS and ISEE-1 satellites rose steadily during the first months in space to values on the order of six times the laboratory value. This was believed to be caused by pre-launch gas contamination of the probe surface. Furthermore, it was found that photoemission could also be drastically reduced in the presence of atmospheric oxygen, and that this effect lasted even some time after the spacecraft had left the oxygen-rich region.

In addition to the photoelectron yield, the energy distribution of the emitted electrons also showed some deviations from the model by Grard. A fit of the

---

[3]It is worth noting here that the shielding may be entirely dominated by the contribution from the photoelectrons themselves, for which there is no clearly defined density at infinity and hence no simple Debye length.

[4]Further complications may arise if the probe surface is not perfectly convex, but has local concavities that may obstruct even very energetic photoelectrons from escaping.
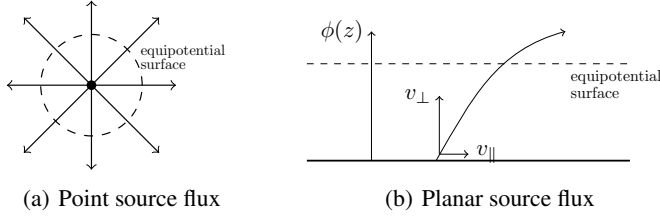
(a) Point source flux　　　　(b) Planar source flux

Figure 3.3. Illustration of photoelectron trajectories for point-like and infinite planar probes.
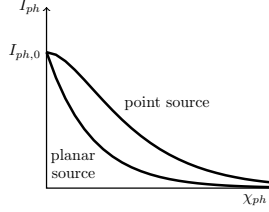

Figure 3.4. Illustration of the photoelectron current-voltage characteristics from point-like and infinite planar probes.

data from ISEE-1, GEOS and GEOTAIL produced the following formula for the photoelectron current density outside the Earth's atmosphere, at a distance of 1 AU from the Sun (Pedersen, 1995):

$$J_{\mathrm{ph}} = 80(\mu\mathrm{Am}^{-2})\exp\{-U_B/2\} + 3(\mu\mathrm{Am}^{-2})\exp\{-U_B/7.5\}. \qquad (3.18)$$

In analogy with Equation (3.17), each of the exponential terms in Equation (3.18) can be interpreted as originating from a Maxwellian population of photoelectrons with temperature $k_B T_{\mathrm{ph}}/e$ equal to the e-folding energy. The first term has an e-folding energy of 2 V that corresponds well to the value predicted by Grard. However, the second term indicates the presence of a hot electron component with a temperature on the order of 7.5 eV, which dominates the photoelectron current at probe potentials greater than about 10 V.

The conclusion of all of this is that photoemission in space is a very complex process that can be influenced by many different factors, both intrinsic and external. While the model and values given by Grard provide a nice framework and basic theoretical understanding, they must be complemented by measurements in space in order to obtain sufficiently accurate models.

3.4 Total probe currents

For a sunlit probe in a space plasma, the total current from the probe to the plasma is typically dominated by the contributions due to impacts of ambient

electrons and ions and the photoelectron current, described in Sections 3.2 and 3.3. In some cases, there are other processes that may give significant contributions to the total current, such as *secondary electron emission* and *electron backscattering*. Secondary electron emission refers to the process by which impacting particles may induce the emission of electrons from the probe surface. If some or all of these *secondary electrons* have enough energy to escape the potential well of the probe[5], they will give rise to a current component in the opposite direction of the electron flow, i. e. *towards* the probe. Electron backscattering is when ambient electrons that hit the probe surface bounce off of it rather than be absorbed by it. This will result in a reduced electron current with respect to the ideal OML electron current, equivalent to an additional current *towards* the probe. Thus, the total probe current can be written (Garret and Whittlesey, 2000)

$$I_{\text{tot}} = I_e + I_i + I_{\text{ph}} + I_{\text{s}e} + I_{\text{s}i} + I_{\text{b}e}, \tag{3.19}$$

where I_e, I_i and I_{ph} are the ambient electron and ion currents and the photoelectron current, respectively. $I_{\text{s}e}$ and $I_{\text{s}i}$ are the current components due to emission of secondary electrons by impacts of ambient electrons and ions, respectively, and $I_{\text{b}e}$ is the current due to backscattered ambient electrons. With the definition of positive current *outwards* from the probe, I_e will be positive and all the other terms on the right-hand side of Equation (3.19) will be negative.

All of the current components in Equation (3.19) depend on the potential of the probe with respect to the plasma, U_B. An unconnected probe will collect current and accumulate charge until the probe potential is such that all the current components cancel out and the total probe current vanishes. This potential is called the *floating potential* of the probe, V_F.

As mentioned above, in the typical case the total probe current is dominated by the ambient electron and ion currents together with the photoelectron current. In fact, since the ions are much heavier than the electrons and hence much less mobile, the ion current is often negligible too, unless the drift velocity of the plasma is very high. The current-voltage characteristics, or *I-V curve*, of the probe in this situation is illustrated in Figure 3.5. For positive probe potentials the photoelectron current falls off exponentially (c. f. Equations (3.16) and (3.17)) and the current due to ambient electrons dominates completely. For negative probe potentials, it is the ambient electron current that decreases exponentially (c. f. Equation (3.3)) and the photoelectron current prevails.

For a sunlit probe in an stationary plasma, the floating potential will be given by the balance between the ambient electron and photoelectron currents, as illustrated in Figure 3.5. The ambient electron current scales with the density of the surrounding plasma (c. f. Equation (3.4)), whereas the pho-

---

[5]Additional constraints may apply in the case of non-point-like probe geometries, as was discussed in Section 3.3 with regards to the photoelectron current.
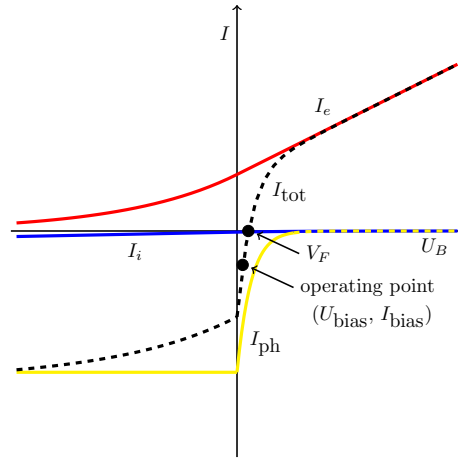
Figure 3.5. Current-voltage characteristics of a spherical probe in a stationary plasma.

toelectron current mainly scales with the intensity of the incident sunlight (c. f. Equation (3.12)). Thus, in dense plasmas and/or far from the sun, where photoemission is weak, the current balance will tend to occur at *negative* probe potentials, where the photoelectron current is saturated and the ambient electron current decreases exponentially. In tenuous plasmas, and/or close to the Sun where photoemission is strong, it will typically happen at *positive* potentials, where the ambient electron current is amplified by the potential field of the probe and the photoelectron current decreases exponentially. *Shaded* probes float when the *ion current* balances the electron current. This typically only happens at large negative potentials, since a strong potential well is needed to compensate for the poor mobility of the much heavier ions.

3.5 Spacecraft charging

A very important phenomenon for in situ measurements in space plasmas is the charging of the spacecraft itself. Qualitatively, the spacecraft behaves very similar to a probe, in the sense that it also exchanges currents with the surrounding plasma. Impacts of ambient plasma particles and emission of photoelectrons are as relevant to any spacecraft surfaces that are exposed to the surrounding space environment as they are to a probe. In the absence of an ion or electron source onboard the spacecraft, that can be used to balance these currents, this will lead to charge build-up on these surfaces. Each equipotential surface will obtain a floating potential depending on its photoemission properties and coupling to the ambient plasma. Having insulating materials or many different equipotential surfaces on a spacecraft can therefore be very dangerous, since the differential charging of these surfaces may give rise to large potential differences between different parts of the spacecraft. This can

34

lead to discharges that are strong enough to damage vital electronics and it may also result in a very complicated and unpredictable potential structure around the spacecraft, which could seriously disturb any measurements of the ambient plasma properties. Because of this, spacecraft are typically designed with a conductive chassis that effectively distributes the charge across the entire surface. This chassis will then be an equipotential, the potential of which is referred to as the *spacecraft potential*.

The spacecraft potential can in principle be found in the same way as the floating potential of a probe: Solving Equation (3.19) for $I_{\text{tot}} = 0$ gives the potential at which all the different current components balance each other and is the potential obtained by a floating object in steady state. However, the complicated geometry of most spacecraft means that the individual terms in Equation (3.19) are not given by the simple expressions used for spherical probes. In fact, analytical solutions are generally not available and one has to resort to numerical simulations to find the expected spacecraft potential in any particular space environment.

The fact that the spacecraft chassis is an equipotential, and typically much larger than any payload instrument, makes it the natural choice of electrical ground for the instruments onboard. Thus, when measuring or biasing the potential of a probe, the spacecraft potential is the reference to which the probe potential is related. For this to work, it is important that the spacecraft surface area is much larger than the surface area of the probes, since otherwise probe currents and voltages may significantly affect the total charge, and hence the potential, of the spacecraft.

Like all charged bodies in a plasma, the spacecraft will be surrounded by a sheath of thickness on the order of the Debye length (Chen, 1984). Inside this sheath, the electric potential and the densities of electrons and ions will be perturbed with respect to the ambient plasma due to the spacecraft charge. If a probe is located inside this sheath, these effects may give rise to erroneous measurements. Specifically, the spacecraft sheath may modify the current-voltage characteristics of the probe. This effect was studied by Olson et al. (2010) for a negatively charged spacecraft. An illustration of the situation is shown in Figure 3.6. In this example, the probe of radius r_{LP} is positively charged and will hence attract electrons. But since it is located inside the sheath of the negatively charged spacecraft, assumed here to be spherical with radius r_{SC} for simplicity, there will be a potential barrier U_{M} that the electrons have to overcome in order to reach the probe. Once across this barrier, the electrons will feel the potential $U_{\text{LP}} + U_{\text{M}}$ and be drawn towards the probe.

Olson et al. suggested that the ambient electron current from a positive probe inside the sheath of a negatively charged spacecraft could be approximated by the OML formulas (Equations (3.3) and (3.4)) with the probe-plasma potential U_B replaced by $U_{\text{LP}} + U_{\text{M}}$ and the electron density n_e replaced by $n_e \exp\left\{-(U_M - U_{\text{pl}})/(k_B T_e)\right\}$, using the terminology of Figure 3.6. In other words, the probe is assumed to draw orbit-limited current from the population
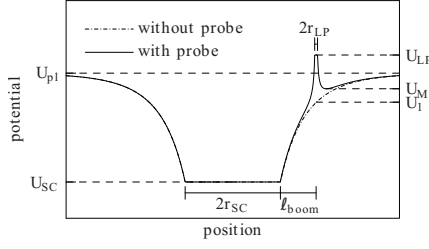
Figure 3.6. Positive probe inside the sheath of a negatively charged spacecraft. The solid curve shows the total potential of the spacecraft and probe; the dashed-dotted curve shows the potential contribution of the spacecraft alone. *(Adapted from Olson et al. (2010).)*

of electrons at the bottom of the potential well U_M, where the density is assumed to obey the *Boltzmann relation* (Chen, 1984) with respect to the plasma outside the spacecraft sheath.

For a negatively biased probe, or a probe at very large positive potential, Olson et al. argued that the potential barrier U_M and Boltzmann factor $\exp\{-(U_M - U_{pl})/(k_B T_e)\}$ are negligible and that the probe current is given to a good approximation by the ideal OML formulas.

The above model, although perhaps not quantitatively very accurate, serves well to demonstrate the physical effects of having a probe inside a spacecraft sheath. The usual way to mitigate these effects is to mount the probe on a boom attached to the spacecraft, so that it may be placed outside of the spacecraft sheath. Of course, these booms may themselves influence the probe measurements, as will be further discussed in the next section.

Double-probe electric field measurements

One of the most important uses of conductive probes in space physics is to measure electric fields in space plasmas. This can be done rather straightforwardly with two probes, by simply immersing them in the plasma and measuring the potential difference between them. The electric field component along the line of probe separation can then be obtained. In the simplest of models, this is trivially computed by dividing the potential difference between the probes, ΔV, by the probe separation distance d:

$$E_{\mathbf{d}} = \frac{\Delta V}{d}. \tag{3.20}$$

This admittedly naïve model is actually the one used in practice, although there are several conditions that have to be met in order for it to be valid. First of all, the probe potentials are not equal to the potentials in the plasma at the respective locations of the probes. Rather, the probe-plasma coupling will

follow the current-voltage characteristics discussed in the previous section and there will be a voltage U_B between each probe and the plasma surrounding it, depending on the currents to and from the probe. This is illustrated in Figure 3.7. Thus, the actual potential difference $\Delta\Phi$ in the plasma is given by

$$\Delta\Phi = (V_2 - U_{B,2}) - (V_1 - U_{B,1}) = \Delta V - (U_{B,2} - U_{B,1}), \qquad (3.21)$$

where $U_{B,1}$ and $U_{B,2}$ are the probe-plasma voltages of probes 1 and 2, respectively. From Equation (3.21) it can be surmised that the naïve model of Equation (3.20) is only valid when $U_{B,1} = U_{B,2}$, i. e. when the probe-plasma coupling is the same for both probes.

The voltages between the probes and the plasma can be controlled by applying a *bias current* I_{bias} to each probe by means of a high-impedance current generator. In the absence of ambient electric fields, this will produce a probe potential U_{bias} with respect to the plasma given by the current-voltage characteristics of the probe. Together, U_{bias} and I_{bias} determine the *operating point* of the probes. An important issue for double-probe electric field measurements is that variations in the probe currents due to local fluctuations in plasma density may significantly affect the probe potentials and give rise to spurious electric fields in the measurement data. The bias current is chosen so as to minimize such effects, by establishing an operating point around which the probe potential is to good approximation independent of the plasma density. In tenuous plasmas, where the probe current is dominated by photoemission and ambient electrons, the optimal operating point in this regard is located on the steep part of the I-V curve, shown in Figure 3.5, where the impedance is low. However, since this low impedance probe-plasma coupling is caused by the steep cut-off of the photoelectron current at positive potentials, this means that reliable double-probe electric field measurements are only feasible if both probes are sunlit. In dense plasmas, where probe photoemission currents are small compared to the ambient electron and ion currents, the best approach is actually to let the probes float (in principle equivalent to $I_{\text{bias}} = 0$). This is because the floating potential V_F is set by the balance of the electron and ion currents, both of which are directly proportional to the plasma density. Thus, provided that the energy distributions of the electrons and ions do not change appreciably, V_F will not change in response to density fluctuations.

As mentioned above, the potentials $U_{B,1}$ and $U_{B,2}$ of the two probes with respect to the ambient plasma have to be equal for Equation (3.20) to be applicable. In practice, this is typically achieved by biasing them with the same current I_{bias}. Then, as long as the current variations due to plasma density fluctuations and potential variations due to the ambient electric fields are small enough that the probes remain on the steep-slope part of the I-V curve, the probe-plasma voltages $U_{B,1}$ and $U_{B,2}$ will be approximately equal. The fidelity of this approach is of course contingent on the requirement that both probes have the same current-voltage characteristics with respect to the ambi-
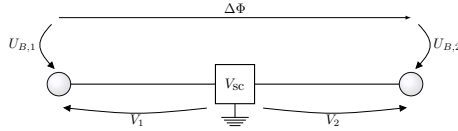
Figure 3.7. Schematic illustration of double-probe electric field measurements.

ent plasma. This in turn requires that the probes be equally shaped and made up of the same material. In the case of a spinning spacecraft, both probes must be spherical so that their sunward projected areas are always equal, otherwise their photoelectron currents will vary with their attitude with respect to the Sun and hence with the spacecraft spin. Clearly, these constraints are less severe for floating probes in dense plasmas, where the effect of the photoemission current on the probe potential is negligible.

The presence of the booms on which the probes are mounted may also be a perturbing factor for electric field measurements. The most prominent example of this is the fact that low energy photoelectrons emitted by the probes, that would normally be attracted back to the respective probes, may be absorbed by the booms instead. This effect is negligible for a sunward probe, since in that case the illuminated surface from which the photoelectrons are emitted is on the opposite side of the probe with respect to the boom. However, for an anti-sunward probe the photoelectrons are emitted in the direction of the boom on which it is mounted and the photoelectron loss to this boom may be significant. This will cause the photoelectron current from that probe to increase, thereby increasing the resulting probe potential for a given bias current I_{bias}. Thus, there will be a potential difference between the probes that is *not* due to an ambient electric field. Direct application of Equation (3.20) will then result in a spurious electric field, directed *towards* the sun since the anti-sunward probe is the one with the higher potential.

3.6 Electron density from spacecraft potential measurements

As mentioned above, for double-probe electric field measurements the probes are biased to an operating point on the steep low-impedance part of the current-voltage characteristics, where the probe-plasma potential is insensitive to current variations due to plasma density fluctuations. The steepness of the curve in this region is a consequence of the rapid decay of the photoelectron current for positive probe potentials. As discussed in Section 3.3, the e-folding energy of the photoelectrons is on the order of 1.5 eV for most materials. This means that the appropriate bias potential will also be of this magnitude. An important consequence of the biasing is therefore that the probe potential will closely follow that of the plasma, except for a small constant offset. Since the

probe potential is measured with respect to the potential of the spacecraft (e. g. V_1 in Figure 3.7), the negative of the probe potential $(-V_1)$ gives a good estimate of the spacecraft potential with respect to the plasma.

Unlike a biased probe, the potential of a *floating* probe will be very susceptible to fluctuations in plasma density, owing to the fact that the ambient electron current is proportional to the plasma (electron) density. In particular, the *spacecraft*, which behaves essentially as a floating probe, will also be sensitive to these fluctuations. Thus, it is possible to use the spacecraft potential as a proxy for measuring the electron density in the surrounding plasma.

The proportionality of the ambient electron current to the plasma density implies that I_e for the spacecraft can be expressed as

$$I_e = n \cdot f\left(V_{sc}/T\right) \tag{3.22}$$

where f contains the dependence on spacecraft potential and plasma temperature. This dependence can be rather complicated in the general case since spacecraft geometries can be quite complex. For a sunlit spacecraft, the floating potential will be given by the balance between the ambient electron current and the photoelectron current. Denoting the latter by $I_{ph}\left(V_{sc}/T_{ph}\right)$ for generality with respect to potentially complicated photoelectron current-voltage relationships, the current balance can be written

$$n \cdot f\left(V_{sc}/T\right) = I_{ph}\left(V_{sc}/T_{ph}\right). \tag{3.23}$$

Solving for the electron density gives

$$n = \frac{I_{ph}\left(V_{sc}/T_{ph}\right)}{f\left(V_{sc}/T\right)}. \tag{3.24}$$

If the functional dependencies $f\left(V_{sc}/T\right)$ and $I_{ph}\left(V_{sc}/T_{ph}\right)$ can be found, either analytically, numerically or empirically, it is thus possible to calculate the electron density from the spacecraft potential using Equation (3.24). Pedersen (1995) found that the spacecraft ambient electron and photoelectron current-voltage characteristics of GEOS-1, GEOS-2 and ISEE-1 were all well approximated by the corresponding formulas for spherical probes of equal sunlit projected area A_p, presented in Sections 3.2 and 3.3. In that case, f and I_{ph} are well known and the electron density can easily be computed from analytical expressions.

4. Particle measurements in space plasmas

4.1 Introduction

Having treated the theory and operations of Langmuir probes rather thoroughly in the previous Chapter, the attention is now shifted to another kind of instrument often of great importance to this thesis: particle spectrometers. The focus of this Chapter is on the electrostatic analyzer, magnetic momentum analyzer and their "combination" in the form of the Wien filter, since instruments of these types are carried by the Rosetta spacecraft.

4.2 The electrostatic analyzer

An electrostatic analyzer sorts incoming particles according to their energy-by-charge ratio by deflecting them in an *electric field*. Typically, a *filter* approach is used in which only particles with a certain energy-to-charge ratio will be deflected in such a way that they pass the filter. An example of this is shown in Figure 4.1 where the incoming particles are funneled through a curved passage, in the form of a circular segment, bounded by two electrical conductors maintained at different potentials. For an incoming particle to pass though the device, its velocity **v** has to be exactly right so that the centripetal force of the circular motion exactly equals the central force on the particle caused by the **E**-field between the plates:

$$\frac{mv^2}{R} = qE. \tag{4.1}$$

Denoting the kinetic energy of the particle by W, the energy-to-charge ratio can be solved for:

$$\frac{W}{q} = \frac{1}{2}ER. \tag{4.2}$$

Thus, the energy to charge ratio that the particles must have in order to pass the filter depends on the electric field E between the plates and the radius of curvature R of the passage. By sequential variation of the electric field, the number of incoming particles per unit time can be obtained as a function of energy-to-charge ratio. As a result, the electrostatic analyzer provides the distribution of energy-to-charge ratios for the subset of particles in the ambient plasma that
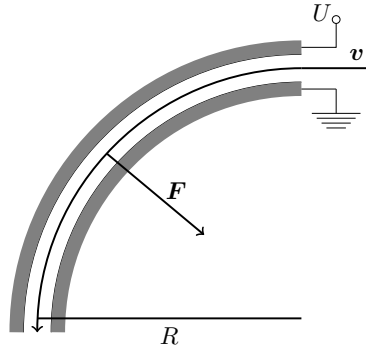
Figure 4.1. Simple schematic of an electrostatic analyzer.

have velocities directed perpendicular to (and in direction *towards*) the instrument aperture. If the plasma is isotropic, this distribution will be equal to the total energy-to-charge distribution of the plasma. However, in the general case of an anisotropic plasma, the aperture has to be either expanded to cover a larger interval of solid angles, or rotated, in order to sample a larger domain of velocity space. In most cases, a combination of these two approaches is used. Perhaps the most important example of this is the *hemispherical top hat* design, shown in Figure 4.2, where cylindrical symmetry is used to achieve a $360°$ omnidirectional field of view in one plane. A voltage on the top guiding plate can be used to efficiently funnel the incoming particles into the slit. The full three-dimensional distribution may then be obtained as the spacecraft on which the instrument is mounted rotates around an axis normal to the axis of symmetry of the instrument. It is also possible to use slanted guiding plates (the dashed lines in Figure 4.2) to increase the field of view somewhat in the vertical direction. A varying guiding plate voltage can then be used to guide particles of different vertical incident angles into the slits, thereby maintaining the ability of the instrument to distinguish between incoming particles from different vertical directions. In order to distinguish between incoming particles from different *azimuthal* directions, the circular detector can be divided up into different segments, each collecting particles from a narrow azimuthal field of view.

4.3 The magnetic momentum analyzer

A magnetic momentum analyzer sorts the incoming particles by deflecting them in a *magnetic field*. The force on a charged particle in a homogeneous magnetic field is given by Lorentz' force law:

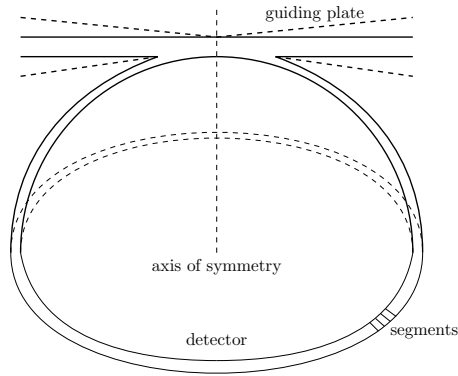$$\mathbf{F} = q\mathbf{v} \times \mathbf{B}. \tag{4.3}$$

41

Figure 4.2. Simple schematic of the geometry of a hemispherical top hat electrostatic analyzer.

Since the magnetic force is proportional to the *velocity* of the particle in addition to the field strength, one power of *v* cancels when equating the magnetic force with the centripetal force, giving

$$\frac{mv}{q} = RB. \tag{4.4}$$

Thus, the *momentum*-to-charge ratio determines whether an incoming particle passes the filter and reaches the detector. Alternatively, a spatially extended detector can be used which, if segmented in analogy with Figure 4.2, allows simultaneous measurement of multiple momentum-to-charge ratios.

4.4 The Wien filter

A combination of electric and magnetic fields can be used to sort incoming particles based on *velocity*. If the instrument is constructed in such a way that only particles that experience no deflection can pass the filter and reach the detector, as shown in Figure 4.3, the balance between electric and magnetic forces can be used to obtain their velocity:

$$q\mathbf{E} = q\mathbf{v} \times \mathbf{B}. \tag{4.5}$$

Assuming $\mathbf{E}$, $\mathbf{v}$ and $\mathbf{B}$ to be perpendicular for simplicity gives
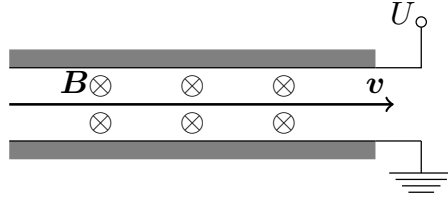
$$v = \frac{E}{B}. \tag{4.6}$$

Figure 4.3. Wien filter schematic. Only particles whose velocity is such that the magnetic force exactly equals the electric force will be able to pass the filter without being deflected onto the electrodes.

Wien filters are often used together with an electrostatic analyzer, since knowing W/q and v gives the *mass*-to-charge ratio:

$$\frac{m}{q} = \frac{W/q}{v^2}. \tag{4.7}$$

The combined instrument is therefore referred to as a *mass analyzer*.

In the case of a curved geometry, the electric and magnetic forces together must equal the centripetal force for a particle to pass through:

$$\frac{mv^2}{R}\hat{\mathbf{r}} = q(\mathbf{E} + \mathbf{v} \times \mathbf{B}). \tag{4.8}$$

For Equation (4.8) to hold, $\mathbf{E}$ must be parallel to $\hat{\mathbf{r}}$, i.e. point inwards towards the center of curvature (or, possibly, outwards, depending on the direction of $\mathbf{B}$), and since $\mathbf{v}$ is tangential to the curved trajectory for any detected particle, $\mathbf{B}$ must be perpendicular to both $\mathbf{v}$ and $\hat{\mathbf{r}}$, i.e. point into or out of the page in Figure 4.1. Choosing inwards as the positive direction for $\mathbf{E}$ and *into* the page as positive for $\mathbf{B}$, Equation (4.8) becomes

$$v^2 - \frac{qR}{m}(E + vB) = 0, \tag{4.9}$$

which is a quadratic equation that can easily be solved for v. Together with an electrostatic analyzer that gives W/q, the mass-to-charge ratio can be obtained.

5. Rosetta: Mission and payload

The European Space Agency's Rosetta mission (Glassmeier et al., 2007a) is the closest and longest investigation of a cometary nucleus ever, and the first to deploy a lander on the surface. The primary objective of the mission is to study the structure, composition and morphology of the nucleus, with the eventual goal of learning more about the formation and early evolution of the solar system from this potentially primordial body. Supplementary goals include the development of cometary activity, dynamics and interaction of gas and dust in the cometary coma, and processes in the cometary plasma environment and its interaction with the solar wind. For these purposes, the spacecraft carries a payload of 11 different instruments (c. f. Figure 5.1 and Table 5.1) and a lander, Philae, with a payload of 10 additional instruments (not shown).

The Rosetta Plasma Consortium (RPC) includes 5 instruments designed to probe the cometary plasma environment:

- The **I**on **C**omposition **A**nalyser (RPC-ICA), a combined electrostatic and magnetic momentum analyzer for ions. Measures the three-dimensional distribution of positive ions in the energy range 25 eV - 40 keV with mass resolution good enough to resolve the major ion species, e. g. H, He, O, O_2, H_2O etc. (Nilsson et al., 2007).
- The **I**on and **E**lectron **S**ensor (RPC-IES), consisting of two electrostatic analyzers, one for ions and one for electrons. Measures three-dimensional distributions of ions (including negative) and electrons, covering an energy-to-charge range of 1 eV/e - 18 KeV/e (Burch et al., 2007).
- The **La**ngmuir **P**robe instrument (RPC-LAP), consisting of two spherical 2.5-cm diameter Langmuir probes mounted on the edges of booms at 2.24 m and 1.62 m distances ouside the orbiter, respectively. Possible measurements include plasma density (1 - 10^6 cm^{-3}), electron temperature ($\sim$ 10 meV - 10 eV), plasma flow velocity ($\lesssim$ 10 km/s), spacecraft potential ($\pm$40 V), electric field fluctuations ($\lesssim$ 8 kHz) and integrated EUV flux (for $n_e \lesssim 1000$ cm^{-3}) (Eriksson et al., 2007).
- The Fluxgate **Mag**netomter (RPC-MAG), a tri-axial fluxgate magnetometer mounted on a 1.5 m boom outside the orbiter. Measures magnetic fields in three dimensions in the frequency range 0-10 Hz (Glassmeier et al., 2007b).
- The **M**utual **I**mpedance **P**robe (RPC-MIP), consisting of two receiving and two transmitting electrodes on a 1-m long bar. Measures the electron density, temperature, plasma drift velocity and wave activity from the mutual impedance frequency response (Trotignon et al., 2007), for Debye lengths of 0.5 - 200 cm.

This thesis primarily makes use of data from RPC-LAP, RPC-ICA and, for context, the ROSINA **Co**metary **P**ressure **S**ensor (ROSINA-COPS), consisting of two pressure gauges for measuring the density and velocity of the neutral gas.

Rosetta's target comet, 67P/Churyumov-Gerasimenko (hereafter 67P), is a Jupiter family comet discovered in 1969. It was put on its current orbit, with an orbital period of 6.5 years and perihelion and aphelion distances of 1.2 AU and 5.6 AU, respectively, by a close encounter with Jupiter in 1959. It is bilobed (c. f. Figure 5.2), approximately 4 km across and has a rotation period of 12.4 hours with a spin axis right ascension of 69 degrees and declination of 64 degrees (Sierks et al., 2015). The shape and spin axis orientation of the nucleus produces great diurnal and seasonal variations of the outgassing and activity as the solar insolation varies over the nucleus surface.

Rosetta arrived at 67P on August 6, 2014, at a heliocentric distance of 3.6 AU. It deployed the lander Philae on November 12, 2014, and has since followed it through perihelion on August 13, 2015, at cometocentric distances mostly on the order of a few tens to a few hundreds of km. It continues to follow the comet as it move away from the Sun, until September 2016 when the mission is set to end with a touchdown on the nucleus surface.
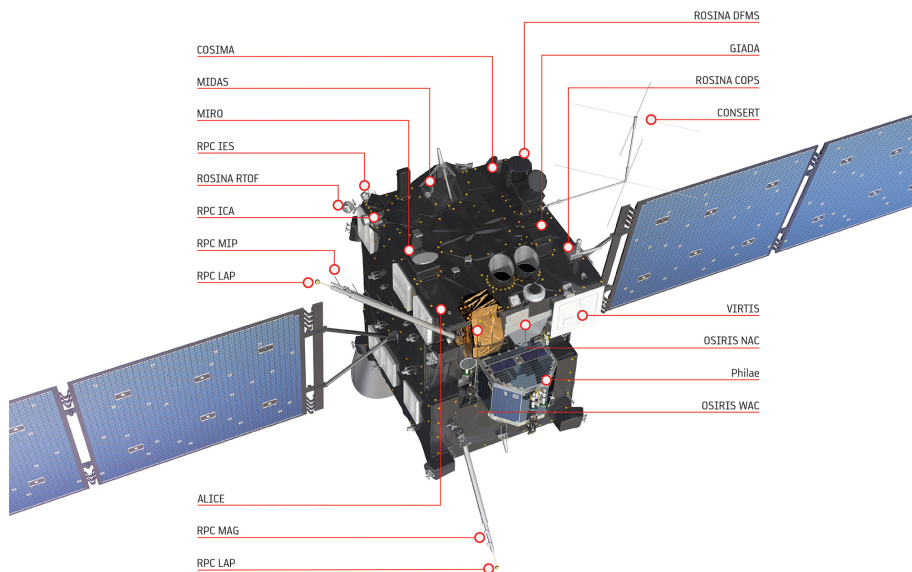
Figure 5.1. Rosetta instruments.

Alice	Ultraviolet Imaging Spectrometer	Stern et al. (2007)
CONSERT	**Co**met **N**ucleus **S**ounding **E**xperiment by **R**adio wave **T**ransmission	Kofman et al. (2007)
COSIMA	**Co**metary **S**econdary **I**on **M**ass **A**nalyser	Kissel et al. (2007)
GIADA	**G**rain **I**mpact **A**nalyser and **D**ust Accumulator	Colangeli et al. (2007)
MIDAS	**M**icro-**I**maging **D**ust **A**nalysis **S**ystem	Riedler et al. (2007)
MIRO	**M**icrowave **I**nstrument for the **R**osetta **O**rbiter	Gulkis et al. (2007)
OSIRIS	**O**ptical, **S**pectroscopic and **I**nfrared **R**emote **I**maging **S**ystem	Keller et al. (2007)
-NAC	**N**arrow **A**ngle **C**amera	
-WAC	**W**ide **A**ngle **C**amera	
ROSINA	**R**osetta **O**rbiter **S**pectrometer for **I**on and **N**eutral **A**nalysis	Balsiger et al. (2007)
-COPS	**Co**metary **P**ressure **S**ensor	
-DFMS	**D**ouble **F**ocussing Mass **S**pectrometer	
-RTOF	**R**eflection **T**ime of **F**light mass spectrometer	
RPC	**R**osetta **P**lasma **C**onsortium	Carr et al. (2007)

Table 5.1. *Rosetta instrument full names and references to instrument descriptions.*
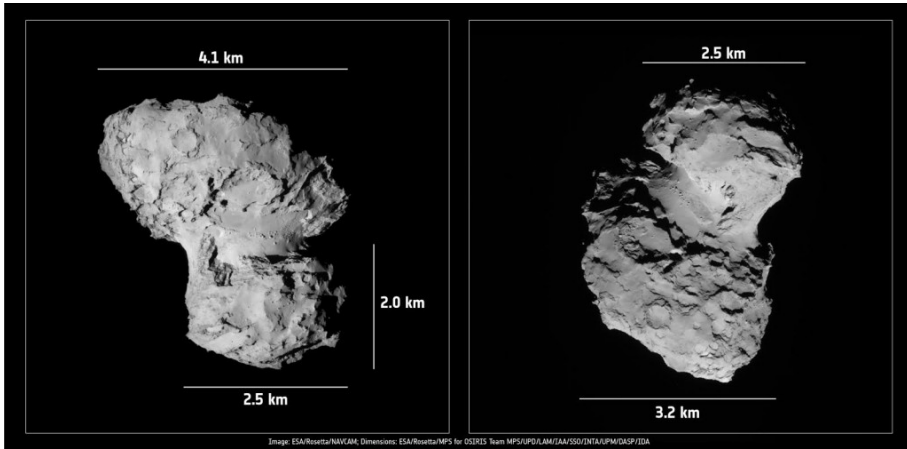
Figure 5.2. Rosetta's target comet, 67P/Churyumov-Gerasimenko.

6. Summary of publications

6.1 Summary of Paper I

In general, it has been difficult to obtain consistent, reliable and accurate estimates of plasma densities and temperatures by the Langmuir probes in the highly variable and dynamic plasma environment and in the presence of a strongly charged spacecraft. Over longer periods of time, the most consistent and reliable measurements are actually the spacecraft potential obtained from the photoelectron knee in the Langmuir probe sweeps. The spacecraft potential is set by the balance of currents due to impacting plasma electrons and emitted photoelectrons. This means that the spacecraft potential is highly sensitive to the electron density and temperature in the surrounding plasma and be used to monitor the plasma environment. Specifically, the spacecraft potential will scale as the logarithm of the electron flux to the spacecraft (with the sign reversed), which in turn is proportional to the electron density times the square root of electron temperature. In this Paper we use measurements of the spacecraft potential to study the evolution of the plasma environment in the inner coma of of comet 67P (cometocentric distances generally between 10 and 150 km) during the time period from early September 2014 to late March 2015, corresponding to heliocentric distances from about 3.5 AU to 2.1 AU. Due to the high electron temperature of about 5 eV, resulting from the low electron-neutral collision rate in the tenuous neutral gas, the spacecraft potential was negative within about 50 km of the nucleus throughout this period. We found a clear covariation of spacecraft potential with the neutral density as measured by the ROSINA Comet Pressure Sensor (COPS), showing that the neutral gas and the plasma were closely coupled. While this is well known for a fully developed comet like 1P/Halley, it was not obvious that it would be the case for the much weaker 67P, particularly early in the mission before any strong boundary layers had formed. We found a clear variation of spacecraft potential with comet longitude, exactly as seen for the neutral gas, already in mid-September 2014, at 3.5 AU heliocentric distance and 30 km from the nucleus. In this sense, 67P had a clear ionosphere of its own, where the local plasma dominates over the solar wind, already at this large distance from the sun. During the investigated period, the comet spin axis was tilted toward the sun, so that the northern hemisphere of the nucleus had summer conditions. As a consequence, the highest electron fluxes and the most negative spacecraft potentials were found in the northern hemisphere. In the northern hemisphere, there was also a clear variation of spacecraft potential with comet longitude,

exactly as seen for the neutral gas. Recurring peaks in density and concurrent dips in spacecraft potential were observed with a period of approximately 6 h, corresponding to half the rotation period of the nucleus. This was found to coincide with sunlit parts of the neck region of the nucleus being in view of the spacecraft.

6.2 Summary of Paper II

Since the charged spacecraft perturbs the potential of the surrounding plasma and the boom length (~ 2 m) is smaller than or comparable to the Debye length ($\sim 1 \text{–} 10$ m for most of the early mission), the Langmuir probe spacecraft potential measurements will only pick up some fraction of the full spacecraft potential. Simulations indicate that, for LAP probe 1 in a tenuous solar wind environment, the fraction of the spacecraft potential measured is on the order 1/2 to 2/3 Sjogren et al. (2012). The spacecraft potential can also be estimated from the ion energy spectra obtained by the Ion Composition Analyzer on the main spacecraft body. Ions entering the instrument have been accelerated by the spacecraft potential and the lowest observed ion energy thus gives an estimate of the spacecraft potential. However, the ion energy spectra suffer from an unknown energy offset, that seems to depend on the sensor temperature. Thus, tThe Langmuir probe instrument measures only a proportion of the full spacecraft potential, while the Ion Composition Analyzer measures the full spacecraft potential, but with an unknown additive offset. In this Paper we combined measurements from both instruments to allow accurate determination of the full spacecraft potential, and how large a fraction of it that is observed by the Langmuir probe instrument.

In the present version of the Paper, we focussed on comparing the LAP1 spacecraft potentials obtained from floating probes in electric field mode, since then the time resolution is much greater and the statistics get much better. Due to a an unfortunate error in our calculations, we erroneously claimed that the fraction of the spacecraft potential picked up in this measurement mode would be the same as the one obtained from the Langmuir probe sweeps in Paper I. This is *not* true, so the results presented in this Paper cannot be directly applied to the Langmuir probe sweeps. However, they are still of course entirely valid for measurements in electric field mode with floating probes. Also, although not shown in the Paper, these measurements actually do agree rather well will the ones obtained from Langmuir probe sweeps in many cases.

We found that the correlation was generally very good between the spacecraft potential estimates obtained from the two instruments, showing clearly that the instruments accurately measure the spacecraft potential. We also found intermittent intervals where the correlation became weaker, typically coinciding with a reduction in the total ion flux observed by ICA and many times also with a drop in the spacecraft potential observed by LAP. We inter-

preted this as a temporary loss of local ionization, in the ambient plasma or at least the ICA field of view. In general, we found that the fraction of the spacecraft potential picked up by LAP was between about 0.7 and 0.9. Thus, applying a correction factor between about 1.1 and 1.4 to the LAP1 floating potential measurements should yield a good estimate of the full spacecraft potential.

References

H. Alfven. On the theory of comet tails. *Tellus*, 9, 1957.

H. Balsiger, K. Altwegg, P. Bochsler, P. Eberhardt, J. Fischer, S. Graf, A. Jäckel, E. Kopp, U. Langer, M. Mildner, J. Müller, T. Riesen, M. Rubin, S. Scherer, P. Wurz, S. Wüthrich, E. Arijs, S. Delanoye, J. de Keyser, E. Neefs, D. Nevejans, H. Rème, C. Aoustin, C. Mazelle, J.-L. Médale, J. A. Sauvaud, J.-J. Berthelier, J.-L. Bertaux, L. Duvet, J.-M. Illiano, S. A. Fuselier, A. G. Ghielmetti, T. Magoncelli, E. G. Shelley, A. Korth, K. Heerlein, H. Lauche, S. Livi, A. Loose, U. Mall, B. Wilken, F. Gliem, B. Fiethe, T. I. Gombosi, B. Block, G. R. Carignan, L. A. Fisk, J. H. Waite, D. T. Young, and H. Wollnik. Rosina Rosetta Orbiter Spectrometer for Ion and Neutral Analysis. *pace Science Reviews*, 128:745–801, February 2007. doi: 10.1007/s11214-006-8335-3.

E. Behar, H. Nilsson, G. S. Wieser, Z. Nemeth, T. W. Broiles, and I. Richter. Mass loading at 67P/Churyumov-Gerasimenko: A case study. *Geophysical Research Letters*, 43:1411–1418, February 2016. doi: 10.1002/2015GL067436.

L. Biermann. Kometenschweife und solare Korpuskularstrahlung. *Zeitschrift für Astrophysik*, 29:274, 1951.

L. Biermann, B. Brosowski, and H. U. Schmidt. The interactions of the solar wind with a comet. *Solar Physics*, 1:254–284, March 1967. doi: 10.1007/BF00150860.

D. Bockelee-Morvan, J. Crovisier, MJ Mumma, and HA Weaver. The composition of cometary volatiles. In M. Festou, H. A. Weaver, and H. U. Keller, editors, *Comets II*, page 391–423. Univ. of Arizona Press, Tucson, 2004.

D. Bockelée-Morvan, V. Debout, S. Erard, C. Leyrat, F. Capaccioni, G. Filacchione, N. Fougere, P. Drossart, G. Arnold, M. Combi, B. Schmitt, J. Crovisier, M.-C. de Sanctis, T. Encrenaz, E. Kührt, E. Palomba, F. W. Taylor, F. Tosi, G. Piccioni, U. Fink, G. Tozzi, A. Barucci, N. Biver, M.-T. Capria, M. Combes, W. Ip, M. Blecka, F. Henry, S. Jacquinod, J.-M. Reess, A. Semery, and D. Tiphene. First observations of H_2O and CO_2 vapor in comet 67P/Churyumov-Gerasimenko made by VIRTIS onboard Rosetta. *Astronomy and Astrophysics*, 583:A6, November 2015. doi: 10.1051/0004-6361/201526303.

J. L. Burch, R. Goldstein, T. E. Cravens, W. C. Gibson, R. N. Lundin, C. J. Pollock, J. D. Winningham, and D. T. Young. RPC-IES: The Ion and Electron Sensor of the Rosetta Plasma Consortium. *Space Science Reviews*, 128:697–712, February 2007. doi: 10.1007/s11214-006-9002-4.

C. Carr, E. Cupido, C. G. Y. Lee, A. Balogh, T. Beek, J. L. Burch, C. N. Dunford, A. I. Eriksson, R. Gill, K. H. Glassmeier, R. Goldstein, D. Lagoutte, R. Lundin, K. Lundin, B. Lybekk, J. L. Michau, G. Musmann, H. Nilsson, C. Pollock, I. Richter, and J. G. Trotignon. RPC: The Rosetta Plasma Consortium. *Space Science Reviews*, 128:629–647, February 2007. doi: 10.1007/s11214-006-9136-4.

F. F. Chen. *Introduction to Plasma Physics and Controlled Fusion*. Plenum Press, New York, 1984.

G. Clark, T. W. Broiles, J. L. Burch, G. A. Collinson, T. Cravens, R. A. Frahm, J. Goldstein, R. Goldstein, K. Mandt, P. Mokashi, M. Samara, and C. J. Pollock. Suprathermal electron environment of comet 67P/Churyumov-Gerasimenko: Observations from the Rosetta Ion and Electron Sensor. *Astronomy and Astrophysicsp*, 583:A24, November 2015. doi: 10.1051/0004-6361/201526351.

A. J. Coates and G. H. Jones. Plasma environment of Jupiter family comets. *Planetary and Space Science*, 57:1175–1191, August 2009. doi: 10.1016/j.pss.2009.04.009.

AJ Coates. Heavy ion effects on cometary shocks. *Advances in Space Research*, 15 (8):403–413, 1995.

L. Colangeli, J. J. Lopez-Moreno, P. Palumbo, J. Rodriguez, M. Cosi, V. Della Corte, F. Esposito, M. Fulle, M. Herranz, J. M. Jeronimo, A. Lopez-Jimenez, E. M. Epifani, R. Morales, F. Moreno, E. Palomba, and A. Rotundi. The Grain Impact Analyser and Dust Accumulator (GIADA) Experiment for the Rosetta Mission: Design, Performances and First Results. *Space Science Reviews*, 128:803–821, February 2007. doi: 10.1007/s11214-006-9038-5.

T. E. Cravens. A magnetohydrodynamical model of the inner coma of Comet Halley. *Journal of Geophysical Research*, 94:15025–15040, November 1989. doi: 10.1029/JA094iA11p15025.

T. E. Cravens. Plasma processes in the inner coma. In R. L. Newburn, Jr., M. Neugebauer, and J. Rahe, editors, *IAU Colloq. 116: Comets in the post-Halley era*, volume 167 of *Astrophysics and Space Science Library*, pages 1211–1255, 1991. doi: 10.1007/978-0-7923-1165-2_50.

L. Dones, P. R. Weissman, H. F Levison, and M. J Duncan. Oort cloud formation and dynamics. In M. C. Festou, H. U. Keller, and H. A. Weaver, editors, *Comets II*, pages 153–174. University of Arizona Press, 2004.

M. Duncan, T. Quinn, and S. Tremaine. The formation and extent of the solar system comet cloud. *The Astronomical Journal*, 94:1330–1338, 1987.

Martin Duncan, Harold Levison, and Luke Dones. Dynamical evolution of ecliptic comets. In M. Festou, H. A. Weaver, and H. U. Keller, editors, *Comets II*, pages 193–204. Univ. of Arizona Press, Tucson, 2004.

Martin J Duncan and Harold F Levison. A disk of scattered icy objects and the origin of jupiter-family comets. *Science*, 276(5319):1670–1672, 1997.

N. J. T. Edberg, A. I. Eriksson, E. Odelstad, P. Henri, J.-P. Lebreton, S. Gasc, M. Rubin, M. André, R. Gill, E. P. G. Johansson, F. Johansson, E. Vigren, J. E. Wahlund, C. M. Carr, E. Cupido, K.-H. Glassmeier, R. Goldstein, C. Koenders, K. Mandt, Z. Nemeth, H. Nilsson, I. Richter, G. S. Wieser, K. Szego, and M. Volwerk. Spatial distribution of low-energy plasma around comet 67P/CG from Rosetta measurements. *Geophysical Research Letters*, 42:4263–4269, June 2015. doi: 10.1002/2015GL064233.

N. J. T. Edberg, A. I. Eriksson, E. Odelstad, E. Vigren, D. J. Andrews, F. Johansson, J. L. Burch, C. M. Carr, E. Cupido, K.-H. Glassmeier, R. Goldstein, J. S. Halekas, P. Henri, C. Koenders, K. Mandt, P. Mokashi, Z. Nemeth, H. Nilsson, R. Ramstad, I. Richter, and G. S. Wieser. Solar wind interaction with comet 67P: Impacts of corotating interaction regions. *Journal of Geophysical Research (Space Physics)*, 121:949–965, February 2016. doi: 10.1002/2015JA022147.

Kenneth Essex Edgeworth. The evolution of our planetary system. *Journal of the British Astronomical Association*, 53:181–188, 1943.

E. Engwall. Cold magnetospheric plasma flows: Properties and interaction with spacecraft. Licentiate thesis, Department of Astronomy and Space Physics, Uppsala University, 2006.

A. I. Eriksson, R. Boström, R. Gill, L. Åhlén, S.-E. Jansson, J.-E. Wahlund, M. André, A. Mälkki, J. A. Holtet, B. Lybekk, A. Pedersen, and L. G. Blomberg. RPC-LAP: The Rosetta Langmuir Probe Instrument. *Space Science Reviews*, 128: 729–744, February 2007. doi: 10.1007/s11214-006-9003-3.

K. A. Farley, A. Montanari, E. M. Shoemaker, and Shoemaker C. S. Geochemical evidence for a comet shower in the late eocene. *Science*, 280:1250–1253, 1998.

J. A. Fernandez. The formation and dynamical survival of the comet cloud. In A. Carusi and G. B. Valsecchi, editors, *Dynamics of Comets: Their Origin and Evolution*, pages 45–70. Reidel, Dordrecht, 1985.

Julio A Fernández. On the existence of a comet belt beyond neptune. *Monthly Notices of the Royal Astronomical Society*, 192(3):481–491, 1980.

K. R. Flammer and D. A. Mendis. A note on the mass-loaded MHD flow of the solar wind towards a cometary nucleus. *Astrophysics and Space Science*, 182:155–162, August 1991. doi: 10.1007/BF00646450.

H. B. Garret and A. C. Whittlesey. Spacecraft Charging, An Update. *IEEE Transactions on Plasma Science*, 28:2017–2028, 2000.

K.-H. Glassmeier, H. Boehnhardt, D. Koschny, E. Kührt, and I. Richter. The Rosetta Mission: Flying Towards the Origin of the Solar System. *Space Science Reviews*, 128:1–21, February 2007a. doi: 10.1007/s11214-006-9140-8.

K.-H. Glassmeier, I. Richter, A. Diedrich, G. Musmann, U. Auster, U. Motschmann, A. Balogh, C. Carr, E. Cupido, A. Coates, M. Rother, K. Schwingenschuh, K. Szegö, and B. Tsurutani. RPC-MAG The Fluxgate Magnetometer in the ROSETTA Plasma Consortium. *Space Science Reviews*, 128:649–670, February 2007b. doi: 10.1007/s11214-006-9114-x.

B. E. Goldstein, K. Altwegg, H. Balsiger, S. A. Fuselier, and W.-H. Ip. Observations of a shock and a recombination layer at the contact surface of Comet Halley. *Journal of Geophysical Research*, 94:17251–17257, December 1989. doi: 10.1029/JA094iA12p17251.

R. Goldstein, J. L. Burch, P. Mokashi, T. Broiles, K. Mandt, J. Hanley, T. Cravens, A. Rahmati, M. Samara, G. Clark, M. Hässig, and J. M. Webster. The Rosetta Ion and Electron Sensor (IES) measurement of the development of pickup ions from comet 67P/Churyumov-Gerasimenko. *Geophysical Research Letters*, 42: 3093–3099, May 2015. doi: 10.1002/2015GL063939.

R. J. L. Grard. Properties of the satellite photoelectron sheath derived from photoemission laboratory measurements. *Journal of Geophysical Research*, 78: 2885–2906, 1973.

S. Gulkis, M. Frerking, J. Crovisier, G. Beaudin, P. Hartogh, P. Encrenaz, T. Koch, C. Kahn, Y. Salinas, R. Nowicki, R. Irigoyen, M. Janssen, P. Stek, M. Hofstadter, M. Allen, C. Backus, L. Kamp, C. Jarchow, E. Steinmetz, A. Deschamps, J. Krieg, M. Gheudin, D. Bockelée-Morvan, N. Biver, T. Encrenaz, D. Despois, W. Ip, E. Lellouch, I. Mann, D. Muhleman, H. Rauer, P. Schloerb, and T. Spilker. MIRO: Microwave Instrument for Rosetta Orbiter. *Space Science Reviews*, 128:561–597,

February 2007. doi: 10.1007/s11214-006-9032-y.

S. Gulkis, M. Allen, P. von Allmen, G. Beaudin, N. Biver, D. Bockelée-Morvan, M. Choukroun, J. Crovisier, B. J. R. Davidsson, P. Encrenaz, T. Encrenaz, M. Frerking, P. Hartogh, M. Hofstadter, W.-H. Ip, M. Janssen, C. Jarchow, S. Keihm, S. Lee, E. Lellouch, C. Leyrat, L. Rezac, F. P. Schloerb, and T. Spilker. Subsurface properties and early activity of comet 67P/Churyumov-Gerasimenko. *Science*, 347(1):aaa0709, January 2015. doi: 10.1126/science.aaa0709.

M. S. Hanner and J. P. Bradley. Composition and mineralogy of cometary dust. In M. Festou, H. A. Weaver, and H. U. Keller, editors, *Comets II*, page 555–564. Univ. of Arizona Press, Tucson, 2004.

M Hässig, K Altwegg, H Balsiger, A Bar-Nun, JJ Berthelier, A Bieler, P Bochsler, C Briois, U Calmonte, M Combi, et al. Time variability and heterogeneity in the coma of 67P/Churyumov-Gerasimenko. *Science*, 347(6220):aaa0276, 2015.

J. Heisler and S. Tremaine. The influence of the galactic tidal field on the oort comet cloud. *Icarus*, 65:13–26, 1986.

J. G. Hills. Comet showers and the steady state infall of comets from the oort cloud. *The Astronomical Journal*, 86:1730–1740, 1981.

S. H. Høymork. *Sensors and Instruments for Space Exploration*. Swedish Institute for Space Physics, Kiruna, 2000.

Y. Itikawa and N. Mason. Cross Sections for Electron Collisions with Water Molecules. *Journal of Physical and Chemical Reference Data*, 34:1–22, March 2005. doi: 10.1063/1.1799251.

H. U. Keller, C. Barbieri, P. Lamy, H. Rickman, R. Rodrigo, K.-P. Wenzel, H. Sierks, M. F. A'Hearn, F. Angrilli, M. Angulo, M. E. Bailey, P. Barthol, M. A. Barucci, J.-L. Bertaux, G. Bianchini, J.-L. Boit, V. Brown, J. A. Burns, I. Büttner, J. M. Castro, G. Cremonese, W. Curdt, V. da Deppo, S. Debei, M. de Cecco, K. Dohlen, S. Fornasier, M. Fulle, D. Germerott, F. Gliem, G. P. Guizzo, S. F. Hviid, W.-H. Ip, L. Jorda, D. Koschny, J. R. Kramm, E. Kührt, M. Küppers, L. M. Lara, A. Llebaria, A. López, A. López-Jimenez, J. López-Moreno, R. Meller, H. Michalik, M. D. Michelena, R. Müller, G. Naletto, A. Origné, G. Parzianello, M. Pertile, C. Quintana, R. Ragazzoni, P. Ramous, K.-U. Reiche, M. Reina, J. Rodríguez, G. Rousset, L. Sabau, A. Sanz, J.-P. Sivan, K. Stöckner, J. Tabero, U. Telljohann, N. Thomas, V. Timon, G. Tomasch, T. Wittrock, and M. Zaccariotto. OSIRIS The Scientific Camera System Onboard Rosetta. *Space Science Reviews*, 128:433–506, February 2007. doi: 10.1007/s11214-006-9128-4.

J. Kissel, K. Altwegg, B. C. Clark, L. Colangeli, H. Cottin, S. Czempiel, J. Eibl, C. Engrand, H. M. Fehringer, B. Feuerbacher, M. Fomenkova, A. Glasmachers, J. M. Greenberg, E. Grün, G. Haerendel, H. Henkel, M. Hilchenbach, H. von Hoerner, H. Höfner, K. Hornung, E. K. Jessberger, A. Koch, H. Krüger, Y. Langevin, P. Parigger, F. Raulin, F. Rüdenauer, J. Rynö, E. R. Schmid, R. Schulz, J. Silén, W. Steiger, T. Stephan, L. Thirkell, R. Thomas, K. Torkar, N. G. Utterback, K. Varmuza, K. P. Wanczek, W. Werther, and H. Zscheeg. Cosima High Resolution Time-of-Flight Secondary Ion Mass Spectrometer for the Analysis of Cometary Dust Particles onboard Rosetta. *Space Science Reviews*, 128:823–867, February 2007. doi: 10.1007/s11214-006-9083-0.

C. Koenders, K.-H. Glassmeier, I. Richter, U. Motschmann, and M. Rubin. Revisiting cometary bow shock positions. *Planetary and Space Science*, 87:85 – 95, 2013.

ISSN 0032-0633. doi: http://dx.doi.org/10.1016/j.pss.2013.08.009. URL `http://www.sciencedirect.com/science/article/pii/S0032063313002146`.

W. Kofman, A. Herique, J.-P. Goutail, T. Hagfors, I. P. Williams, E. Nielsen, J.-P. Barriot, Y. Barbin, C. Elachi, P. Edenhofer, A.-C. Levasseur-Regourd, D. Plettemeier, G. Picardi, R. Seu, and V. Svedhem. The Comet Nucleus Sounding Experiment by Radiowave Transmission (CONSERT): A Short Description of the Instrument and of the Commissioning Stages. *Space Science Reviews*, 128: 413–432, February 2007. doi: 10.1007/s11214-006-9034-9.

Gerard P Kuiper. On the origin of the solar system. *Proceedings of the National Academy of Sciences*, 37(1):1–14, 1951.

J. G. Laframboise and L. W. Parker. Probe design for orbit-limited current collection. *The Physics of Fluids*, 16:629–636, 1973.

H. F. Levison and M. J. Duncan. From the Kuiper Belt to Jupiter-Family Comets: The Spatial Distribution of Ecliptic Comets. *Icarus*, 127:13–32, May 1997. doi: 10.1006/icar.1996.5637.

C. M. Lisse, T. E. Cravens, and K. Dennerl. X-ray and extreme ultraviolet emission from comets. In M. Festou, H. A. Weaver, and H. U. Keller, editors, *Comets II*, pages 631–643. Univ. of Arizona Press, Tucson, 2004.

G Medicus. Theory of electron collection of spherical probes. *Journal of Applied Physics*, 33:2512–2520, 1961.

D. A. Mendis. A postencounter view of comets. *Annual review of astronomy and astrophysic*, 26:11–49, 1988. doi: 10.1146/annurev.aa.26.090188.000303.

H. Mott-Smith and I. Langmuir. The theory of collectors in gaseous discharges. *Physical Review*, 28:727–763, 1926.

H. Nilsson, R. Lundin, K. Lundin, S. Barabash, H. Borg, O. Norberg, A. Fedorov, J.-A. Sauvaud, H. Koskinen, E. Kallio, P. Riihelä, and J. L. Burch. RPC-ICA: The Ion Composition Analyzer of the Rosetta Plasma Consortium. *Space Science Reviews*, 128:671–695, February 2007. doi: 10.1007/s11214-006-9031-z.

H. Nilsson, G. Stenberg Wieser, E. Behar, C. S. Wedlund, H. Gunell, M. Yamauchi, R. Lundin, S. Barabash, M. Wieser, C. Carr, E. Cupido, J. L. Burch, A. Fedorov, J.-A. Sauvaud, H. Koskinen, E. Kallio, J.-P. Lebreton, A. Eriksson, N. Edberg, R. Goldstein, P. Henri, C. Koenders, P. Mokashi, Z. Nemeth, I. Richter, K. Szego, M. Volwerk, C. Vallat, and M. Rubin. Birth of a comet magnetosphere: A spring of water ions. *Science*, 347(1):aaa0571, January 2015a. doi: 10.1126/science.aaa0571.

H. Nilsson, G. Stenberg Wieser, E. Behar, C. S. Wedlund, E. Kallio, H. Gunell, N. J. T. Edberg, A. I. Eriksson, M. Yamauchi, C. Koenders, M. Wieser, R. Lundin, S. Barabash, K. Mandt, J. L. Burch, R. Goldstein, P. Mokashi, C. Carr, E. Cupido, P. T. Fox, K. Szego, Z. Nemeth, A. Fedorov, J.-A. Sauvaud, H. Koskinen, I. Richter, J.-P. Lebreton, P. Henri, M. Volwerk, C. Vallat, and B. Geiger. Evolution of the ion environment of comet 67P/Churyumov-Gerasimenko. Observations between 3.6 and 2.0 AU. *Astronomy and Astrophysics*, 583:A20, November 2015b. doi: 10.1051/0004-6361/201526142.

J. Olson, N. Brenning, J.-E. Wahlund, and H. Gunell. On the interpretation of langmuir probe data inside a spacecraft sheath. *Review of Scientific Instruments*, 81:105106, 2010.

N. Omidi, D. Winske, and C. S. Wu. The effect of heavy ions on the formation and structure of cometary bow shocks. *Icarus*, 66:165–180, April 1986. doi: 10.1016/0019-1035(86)90016-3.

J. H. Oort. The structure of the cloud of comets surrounding the solar system and a hypothesis concerning its origin. *Bulletin of the Astronomical Institutes of the Netherlands*, 11:91–110, 1950.

A. Pedersen. Solar wind and magnetosphere plasma diagnostics by spacecraft electrostatic potential measurements. *Ann. Geophysicae*, 13:118–129, 1995.

D. Prialnik, J. Benkhoff, and M. Podolak. Modeling the structure and activity of comet nuclei. In G. W. Kronk, editor, *Comets II*, pages 359–387. Univ. of Arizona Press, Tucson, 2004.

H. Rickman, M. Fouchard, C. FroeschlÃ©, and G. B. Valsecchi. Injection of oort cloud comets: the fundamental role of stellar perturbations. *Celestial Mmechanics and Dynamical Astronomy*, 102:111–132, 2008.

W. Riedler, K. Torkar, H. Jeszenszky, J. Romstedt, H. S. C. Alleyne, H. Arends, W. Barth, J. V. D. Biezen, B. Butler, P. Ehrenfreund, M. Fehringer, G. Fremuth, J. Gavira, O. Havnes, E. K. Jessberger, R. Kassing, W. Klöck, C. Koeberl, A. C. Levasseur-Regourd, M. Maurette, F. Rüdenauer, R. Schmidt, G. Stangl, M. Steller, and I. Weber. MIDAS The Micro-Imaging Dust Analysis System for the Rosetta Mission. *Space Science Reviews*, 128:869–904, February 2007. doi: 10.1007/s11214-006-9040-y.

Robert Schunk and Andrew Nagy. *Ionospheres: physics, plasma physics, and chemistry*. Cambridge university press, 2009.

Holger Sierks, Cesare Barbieri, Philippe L Lamy, Rafael Rodrigo, Detlef Koschny, Hans Rickman, Horst Uwe Keller, Jessica Agarwal, Michael F A'Hearn, Francesco Angrilli, et al. On the nucleus structure and activity of comet 67P/Churyumov-Gerasimenko. *Science*, 347(6220):aaa1044, 2015.

A. Sjogren, A. I. Eriksson, and C. M. Cully. Simulation of Potential Measurements Around a Photoemitting Spacecraft in a Flowing Plasma. *IEEE Transactions on Plasma Science*, 40:1257–1261, April 2012. doi: 10.1109/TPS.2012.2186616.

S. A. Stern, D. C. Slater, J. Scherrer, J. Stone, M. Versteeg, M. F. A'Hearn, J. L. Bertaux, P. D. Feldman, M. C. Festou, J. W. Parker, and O. H. W. Siegmund. Alice: The rosetta Ultraviolet Imaging Spectrograph. *Space Science Reviews*, 128: 507–527, February 2007. doi: 10.1007/s11214-006-9035-8.

J. G. Trotignon, J. L. Michau, D. Lagoutte, M. Chabassière, G. Chalumeau, F. Colin, P. M. E. Décréau, J. Geiswiller, P. Gille, R. Grard, T. Hachemi, M. Hamelin, A. Eriksson, H. Laakso, J. P. Lebreton, C. Mazelle, O. Randriamboarison, W. Schmidt, A. Smit, U. Telljohann, and P. Zamora. RPC-MIP: the Mutual Impedance Probe of the Rosetta Plasma Consortium. *Space Science Reviews*, 128: 713–728, February 2007. doi: 10.1007/s11214-006-9005-1.

B. T. Tsurutani. Comets - A laboratory for plasma waves and instabilities. *Washington DC American Geophysical Union Geophysical Monograph Series*, 61: 189–209, 1991.

F. L. Whipple. A comet model. I. The acceleration of Comet Encke. *Astrophysical Journal*, 111:375–394, March 1950. doi: 10.1086/145272.

S. Yabushita. On exact solution of diffusion equation in cometary dynamics. *Astronomy and Astrophysics*, 85:77–79, 1980.